Convergence, stability, and variability of shallow water acoustic predictions using a split-step Fourier parabolic equation model

Kevin B. Smith
Department of Physics
Naval Postgraduate School
Monterey, CA 93940
kevin@physics.nps.navy.mil

The Shallow Water Acoustic Modeling (SWAM'99) Workshop was organized to examine the ability of various acoustic propagation models to accurately predict sound transmission in a variety of shallow water environments designed with realistic perturbations. In order to quantify this, tests of reciprocity, convergence, and stability must be considered. This paper presents the results of an established parabolic equation model based on the split-step Fourier algorithm. The test cases examined in this paper include a simple isospeed water column over a flat bottom with geoacoustic parameter variations, a randomly sloping bottom with geoacoustic parameter variations, and a canonical shallow water profile perturbed by internal waves over a flat, homogeneous bottom. Source configurations were generally held constant but numerous single frequency and broadband runs were performed. Model testing is emphasized with specific criteria for accurate solutions being specified. Random perturbations are added to one test case to examine the influence of environmental uncertainty on the details of the propagation. The results indicate that point-wise accurate solutions to the acoustic field in shallow water cannot be achieved beyond a few kilometers. This is partly due to the inaccuracies of the split-step Fourier algorithm employed in these shallow water scenarios and the treatment of the bottom interface boundary conditions, but also due to the inherent variability caused by uncertain environmental specification. Thus, more general features of the acoustic field should be emphasized at longer ranges.

I. Introduction

This paper will present results from a well-established, well-documented parabolic equation (PE) model with solutions based on the highly stable and efficient split-step Fourier algorithm. The purpose of this paper is not to try to present benchmark quality solutions, but to suggest what level of accuracy is possible with such a model, and what its strengths and weaknesses are. We shall limit the majority of this paper to the examination of the FLAT, Case A environment, as defined in the summary paper of the Shallow Water Acoustic Modeling (SWAM'99) Workshop. Details of this scenario will be given in a subsequent section. Results of a few other SWAM'99 environments will also be presented.

In order to make such a case, it is necessary to run the model through a variety of tests. For any given model or environment, a requirement which is easily justified and measurable is a test of reciprocity. Solutions of the acoustic wave equation must satisfy reciprocity if the environment is stationary. This may be formally written as[1]

$$\rho(\vec{x}_2)g(\vec{x}_1,\vec{x}_2) = \rho(\vec{x}_1)g(\vec{x}_2,\vec{x}_1) \tag{1}$$

where $g(\vec{x}_1, \vec{x}_2)$ is the acoustic Green's function measured by a point receiver at position $\vec{x}_1$ due to a point source located at position $\vec{x}_2$, vice-versa for $g(\vec{x}_2, \vec{x}_1)$, and $\rho(\vec{x}_i)$ is the density at the corresponding position. In the water column, we can treat the fluid as incompressible and density is constant. Since the Green's function is directly proportional to the acoustic pressure, Eq. (1) states that the complex acoustic pressure measured at a point receiver at position $\vec{x}_1$ due to a point source located at position $\vec{x}_2$ should be identical to the complex acoustic pressure measured at a point receiver at position $\vec{x}_2$ due to a point source located at position $\vec{x}_1$.

This is a necessary, but not sufficient, condition of any acoustic propagation model. One can also show a similar reciprocity condition holds for broadband pulse responses.[2] However, if this CW condition is satisfied for all frequencies over the bandwidth, then the pulse response condition must also be satisfied and does not provide an additional check of validity of the solution. It is also important to note that this requirement is fundamental to any model that attempts to use the principle of reciprocity for problems associated with matched field processing, transient localization, or tomography.

Another test which should be applied to any acoustic model is that of convergence. Unfortunately, there is no strict definition of convergence. Many people assume that convergence must be attained as the computational mesh size is decreased to ever smaller sizes. However, as will be seen in this analysis, that is not true for the split-step Fourier algorithm because of the structure of the propagator functions which march the solution from one range bin to the next. In addition, the treatment of the bottom interface boundary condition causes some difficulty in obtaining accurate solutions, and the choice of depth mesh size is found to be optimal over a specific finite range of values. Instead, we shall assume a more relaxed definition of convergence in which the solution appears to approach a stable solution as the grid sizes are varied.

This issue of convergence is further complicated by the fact that although the accuracy of a solution at a single depth may improve with smaller depth mesh size, the accuracy of the global solution may not improve. For example, if a solution is desired at a depth which does not coincide with a specific depth grid, an interpolation scheme must be employed to obtain that solution. Such an interpolation scheme introduces its own error which is completely distinct from the convergence of the general solution. Thus, one must consider when the general solution has reached a reasonable level of convergence, and not rely on a single point in range or depth.

In the following section, an overview of the acoustic propagation model and its implementation will be given. Section III will contain results from the FLAT test case defined at the workshop, and the aforementioned tests of the solutions will be considered. The final results will be compared with benchmark quality results provided by another researcher during the workshop. In Section IV, various results from some of the SWAM'99 test cases will be presented, including predictions of broadband pulse propagation. Some final comments on the usefulness of this propagation model will be provided in the Conclusions.

II. Monterey-Miami Parabolic Equation (MMPE) Model

Much of this section has been adapted from the technical report written for the predecessor of the MMPE model.[3] Rather than simply referring to this report, we include the fundamental aspects of the approximation and the details of its implementation, especially the choice of mesh sizes and the treatment of the interfaces. This was felt to be appropriate since the remainder of the paper performs an exhaustive analysis of the influence of this treatment on the accuracy of the solutions.

We begin by representing the time-harmonic acoustic field in a cylindrical coordinate system (r, z, φ) by

$$P(r, z, \varphi, \omega t) = p(r, z, \varphi)e^{-i\omega t} \quad . \tag{2}$$

Substituting this into the wave equation in cylindrical coordinates leads to the Helmholtz equation,

$$\frac{1}{r}\frac{\partial}{\partial r}\left(r\frac{\partial p}{\partial r}\right) + \frac{1}{r^2}\frac{\partial^2 p}{\partial \varphi^2} + \frac{\partial^2 p}{\partial z^2} + k_0^2 n^2(r, z, \varphi)p = -4\pi P_0 \delta(\hat{x} - \hat{x}_S) \tag{3}$$

where $k_0 = \dfrac{\omega}{c_0}$ is the reference wavenumber, $n(r, z, \varphi) = \dfrac{c_0}{c(r, z, \varphi)}$ is the acoustic index of refraction, c_0 is the reference sound speed, and $c(r, z, \varphi)$ is the acoustic sound speed. It is within $c(r, z, \varphi)$ that all features of the environment are represented (except density, which will be added later). The source function is that of a point source at coordinates $(r = 0, z = z_S)$ with reference source level P_0 defined as the pressure amplitude at a reference distance of $R_0 = 1$ m, and

$$\delta(\hat{x}) = \frac{1}{2\pi r}\delta(z - z_S)\delta(r) \tag{4}$$

is the Dirac-delta function defining the point source contribution.

To account for the cylindrical spreading which dominates the propagation and to simplify the form of the Helmholtz equation, we define

$$p(r, z) = \frac{1}{\sqrt{r}}u(r, z) \quad . \tag{5}$$

Substituting this into Eq. (3) (and neglecting the source term) yields

$$\frac{\partial^2 u}{\partial r^2} + \frac{1}{r^2}\frac{\partial^2 u}{\partial \varphi^2} + \frac{\partial^2 u}{\partial z^2} + k_0^2\left(n^2 + \frac{1}{4k_0^2 r^2}\right)u = 0 \quad . \tag{6}$$

The final term in this equation drops off like $1/r^2$ and is generally neglected in the solution. The second term in this equation introduces azimuthal coupling between different radials, and is generally small. Neglect of this term is often referred to as the uncoupled azimuth (UNCA) approximation. However, we shall keep this term for much of the remainder of this development to allow for full three-dimensional (3D) calculations.

The remaining Helmholtz equation can then be factored by introducing the operator notation

$$P_{op} = \frac{\partial}{\partial r} \tag{7}$$

and

$$Q_{op} = (\mu + \varepsilon + \nu + 1)^{1/2} \tag{8}$$

where

$$\varepsilon = n^2 - 1, \ \mu = \frac{1}{k_0^2}\frac{\partial^2}{\partial z^2}, \text{ and } \nu = \frac{1}{k_0^2 r^2}\frac{\partial^2}{\partial \varphi^2} \quad . \tag{9}$$

The homogeneous form of Eq. (3) then becomes

$$(P_{op}^2 + k_0^2 Q_{op}^2)u = 0 \ . \tag{10}$$

Proper factorization of the outward propagating field is obtained by defining[4]

$$u = Q_{op}^{-1/2}\Psi \ . \tag{11}$$

It is important to include the Q_{op} factor, the first order WKBJ approximation, in Eq. (11) for several reasons including proper initial condition of the starting field and power conservation. We also assume the commutator $[P_{op}, Q_{op}]$ is negligible, implying weak range dependence in the environment, and is, in fact, exactly zero in layered media. The outgoing wave then satisfies

$$P_{op}\Psi = ik_0 Q_{op}\Psi \tag{12}$$

or

$$-ik_0^{-1}\frac{\partial \Psi}{\partial r} = Q_{op}\Psi \ . \tag{13}$$

When backscattered energy may be considered negligible, Eq. (13) represents the complete description of the forward propagating acoustic energy in the waveguide. This *parabolic* form of the acoustic wave equation is the foundation for all PE models. What remains is a method for generating solutions to this equation. As we shall see, much of this depends on developing approximations to the pseudo-differential operator Q_{op}.

The Split-Step Fourier Algorithm

In order to develop a numerical algorithm for solving the PE, we begin by recognizing that the acoustic field may be decomposed into a slowly modulating envelope function and a phase term which oscillates at the acoustic frequency. The envelope function, or PE field function $\psi(r, z, \varphi)$, is defined according to

$$\Psi = \psi e^{ik_0 r} \tag{14}$$

or, in terms of the acoustic pressure,

$$p(r, z, \varphi) = P_0\sqrt{\frac{R_0}{r}}Q_{op}^{-1/2}\psi(r, z, \varphi)e^{ik_0 r} \ . \tag{15}$$

This definition is scaled such that at $r = R_0$, $|\psi| = 1$ and $|p| = P_0$. Substitution of this expression into the Helmholtz equation yields the defining PE for the field function,

$$\frac{\partial \psi}{\partial r} = -ik_0\psi + ik_0 Q_{op}\psi = -ik_0 H_{op}\psi \ , \tag{16}$$

where

$$H_{op} = 1 - Q_{op} \tag{17}$$

is a Hamiltonian-like operator which defines the evolution of the PE field function in range.

In Eq. (16), the function ψ is a vector (in z) in Hilbert space. The relationship between the values of ψ at different ranges can now be expressed as

$$\psi(r + \Delta r) = \Phi(r)\psi(r) \ . \tag{18}$$

To propagate the solution out in range requires a representation of the propagator $\Phi(r)$. There are three common methods of computing PE solutions: (1) the split-step Fourier (PE/SSF)

method,[5] (2) the implicit finite difference (IFD-PE) method,[6] and (3) the finite element (FEPE) method.[7],[8] The primary strengths of the PE/SSF implementation of the PE are its speed and simplicity. The computational efficiency of the PE/SSF algorithm is well-known in range-dependent media. Other PE algorithms have been shown to produce more efficient results in range-independent media.[9] However, the primary reason for working with PE approximations is the treatment of general range-dependent environments in which the PE/SSF algorithm retains effectively the same level of efficiency as in range-independent scenarios.

Since the MMPE model uses the first technique, we shall isolate our discussion to the implementation of the PE/SSF method. This is easily accomplished by approximating the propagator function by

$$\Phi(r) \approx e^{-ik_0 \bar{H}_{op}(r)\Delta r} \tag{19}$$

where

$$\bar{H}_{op}(r) \;=\; \frac{1}{\Delta r}\int_r^{r+\Delta r} dr' H_{op}(r') \quad . \tag{20}$$

The formal solution, using a Dyson time evolution operator,[10] would be

$$\psi(r+\Delta r) \;=\; \mathcal{T} e^{-ik_0 \int_r^{r+\Delta r} dr' H_{op}(r')} \psi(r) \tag{21}$$

where

$$\mathcal{T} e^{-ik_0 \int_r^{r+\Delta r} dr' H_{op}(r')} \;=\; 1 - ik_0 \int_r^{r+\Delta r} dr' H_{op}(r') - k_0^2 \int_r^{r+\Delta r} dr' \int_r^{r'} dr'' H_{op}(r'') H_{op}(r') + (\text{higher order terms}) \quad . \tag{22}$$

Thus, from Eqs. (21) and (22), the lowest order correction to Eq. (19) could be evaluated. This author is unaware of any such error analysis having been performed in a range-dependent environment, however.

Finally, the SSF algorithm is based upon the observation that the operators H_{op} and Q_{op} are not simply scalar operators but instead are a combination of scalar and differential operators. However, each individual operator within H_{op} can be efficiently applied by a simple multiplication in the appropriate domain. Thus, it is essential to the SSF algorithm that the different terms within H_{op} be separated. This requires an approximation to the square-root operator, of which there are numerous forms. Within the MMPE model, it is assumed that the azimuthal coupling term is small, and that a binomial expansion is sufficient to incorporate azimuthal coupling. For the remaining terms within the square root, the wide-angle PE

approximation of Thomson and Chapman[11] is employed. Thus, the full approximation for the Hamiltonian operator is

$$H_{op} \approx T_{op} + U_{op} + V_{op} \tag{23}$$

where

$$T_{op} = 1 - \left[1 + \frac{1}{k_0^2}\frac{\partial^2}{\partial z^2}\right]^{1/2} , \tag{24}$$

$$U_{op} = -(n-1) , \tag{25}$$

and

$$V_{op} = -\frac{1}{2k_0^2 r^2}\frac{\partial^2}{\partial \varphi^2} . \tag{26}$$

In this form, both differential operators have been separated from the index of refraction term as required for implementation with the SSF technique.

For the remainder of this discussion, we shall employ the UNCA approximation in which $V_{op} = 0$ identically. The treatment of this operator within the SSF algorithm follows a similar approach as the T_{op} operator and has previously been described in detail.[12],[13] The operator U_{op} is simply a multiplication operator in *z*-space and, hence, is a diagonal matrix. The operator T_{op} is not diagonal in *z*-space so different depth eigenfunctions are coupled. In vertical wavenumber space, however, the corresponding operator T_{op} is diagonal. It is desirable, therefore, to separate the application of each operator, one in *z*-space and one in k_z-space. Using the Baker-Campbell-Hausdorff expansion,[14] we may write

$$e^{A+B} = e^A e^B e^{[A,B] + [A,[A,B]] + [B,[B,A]] + \ldots} \tag{27}$$

where $A = -ik_0 \Delta r T_{op}$ and $B = -ik_0 \Delta r U_{op}$. Since both T_{op} and U_{op} are small then we assume their products are of second order and negligible. An analysis of the lowest order error due to this approximation in range-dependent media has also never been performed. Finally then, we have

$$\Phi(r) = e^{-ik_0 \frac{\Delta r}{2} U_{op}(r+\Delta r)} e^{-ik_0 \Delta r T_{op}} e^{-ik_0 \frac{\Delta r}{2} U_{op}(r)} \tag{28}$$

where error analysis[15] shows that this "centered step" scheme provides third order accuracy in Δr, and is the method used in the MMPE implementation.

Note from Eq. (28) that if there are no losses present (i.e. $ImT_{op} = ImU_{op} = 0$) then

$$||\Phi(r)|| = 1 , \tag{29}$$

and $\Phi(r)$ is a unitary operator. Therefore, the normalization condition for the complete 3-D (or Nx2-D) field function is

$$||\psi(r)|| = \int|\psi(r, z, \varphi)|^2 dz d\varphi = \text{constant} . \tag{30}$$

Tappert[16] has shown this implies, because of the formulation of the propagator, that the PE/SSF scheme is conservative. Specifically, since

$$|\psi|^2 = rp^* Q_{op} p \tag{31}$$

then

$$\int p^* Q_{op} p dz 2\pi r d\varphi = \text{constant} \tag{32}$$

which shows conservation of the radial component of acoustic power. Thus, there are no intrinsic losses due to the numerical scheme and energy conservation is not a concern in this formulation.

The general algorithm behind the PE/SSF implementation is then as follows. The PE field function ψ is specified at some range r in the z-domain. A multiplication of the z-space operator $e^{-ik_0\frac{\Delta r}{2}U_{op}(r)}$ defined at the beginning of the range-step is applied. A transformation is then made to the k_z-domain followed by a multiplication of the k_z-space operator $e^{-ik_0\Delta r\hat{T}_{op}}$. The result is then transformed again to the z-domain followed by a multiplication of the z-space operator $e^{-ik_0\frac{\Delta r}{2}U_{op}(r+\Delta r)}$ defined at the end of the range-step. The final result is the field function at $r + \Delta r$. The discrete fast Fourier transform (FFT) subroutine employed in the numerical code assumes the convention

$$\psi(z) = \text{FFT}(\psi(k_z)) \tag{33}$$

and

$$\psi(k_z) = \text{IFFT}(\psi(z)) . \tag{34}$$

Therefore, the PE/SSF implementation can be represented by

$$\psi(r+\Delta r, z) \;=\; e^{-ik_0\frac{\Delta r}{2}U_{op}(r+\Delta r,\,z)} \times \mathrm{FFT}\left\{ e^{-ik_0\Delta r\hat{T}_{op}(k_z)} \times \mathrm{IFFT}\left[e^{-ik_0\frac{\Delta r}{2}U_{op}(r,\,z)} \times \psi(r, z) \right] \right\} \;, \quad (35)$$

where, in k_z-space,

$$\hat{T}_{op}(k_z) \;=\; 1 - \left[1 - \left(\frac{k_z}{k_0} \right)^2 \right]^{1/2} \quad . \quad (36)$$

Note that modes with $k_z > k_0$ are evanescent since

$$\hat{T}_{op}(k_z > k_0) \;=\; 1 - i\left[\left(\frac{k_z}{k_0} \right)^2 - 1 \right]^{1/2} \quad . \quad (37)$$

In practice, only the real ocean half of the operator U_{op} is required to multiply the real ocean half of ψ. The symmetry condition defined below in Eq. (50) can then be applied prior to transformation to the k_z-domain. Furthermore, between range steps (at the end of one and the beginning of another), two separate applications of the scalar operator $e^{-ik_0\frac{\Delta r}{2}U_{op}(r)}$ are unnecessary, and are combined into a single application with range step Δr.

MMPE Grid Sizes

As in all models, a discretization of the environment is required and defined by the mesh size $(\Delta r, \Delta z)$. The field and the propagator functions then become discretized arrays in depth of length N which defines the size of the FFT used in the SSF algorithm, i.e.

$$\psi(r, z) \Rightarrow \psi(r_i, z_n) \quad (38)$$

where

$$r_i \;=\; (i-1)\Delta r \;,\;\; i \;=\; 1, i_{max} \;, \quad (39)$$

and

$$z_n \;=\; \begin{cases} \left(n - \frac{1}{2} \right)\Delta z \;, & n \;=\; 1, \frac{N}{2} \\ -\left(N - n + \frac{1}{2} \right)\Delta z \;, & n \;=\; \frac{N}{2} + 1, N \end{cases} \quad . \quad (40)$$

Note that the depth mesh is defined such that grid points lie on fractional values of Δz. This convention was introduced to avoid carrying the zero-pressure value at $z = 0$ through the calculation. Furthermore, note that half of the depth mesh values define an "image ocean" for negative depths. This is necessary when using the full Fourier transform and has the added benefit of enforcing the surface boundary condition (to be defined below) through symmetry of the FFT.

Because the depth mesh influences the wavenumber increments Δk_z via the FFT, we may define a default value for Δz, hence the transform size N, by considering a lower limit on allowable angles of propagation. Since N wavenumber values will be spread over the range $+k_{z,max}$ to $-k_{z,max}$, it follows that

$$k_{z,\,max} = \frac{N}{2}\Delta k_z\,,\ \Delta k_z = \frac{2\pi}{z_T}\,, \tag{41}$$

where z_T is the total computational depth (including both real and image ocean), so

$$k_{z,\,max} = \frac{N\pi}{z_T}\ . \tag{42}$$

Furthermore, the vertical wavenumbers are related to the angles of propagation by

$$k_z = k_0 \sin\theta\ . \tag{43}$$

It follows that for a given maximum angle of propagation, the minimum transform size required must satisfy

$$N_{min} \geq \frac{k_0 z_T}{\pi}\sin\theta_{max}\ . \tag{44}$$

To define an upper bound on the range step size, Δr_{max}, Tappert[4] used the analogy of physical optics to obtain an expression for the upper limit on the range step size

$$\Delta r_{max} \leq \frac{2}{k_0 \sin^2\theta_{max}}\ . \tag{45}$$

A similar analysis suggests that the maximum vertical mesh size is given by

$$\Delta z_{max} \leq \frac{2f}{k_0} \sim \frac{2}{k_0 \sin\theta_{max}} \tag{46}$$

which can be shown to yield roughly the same order for the transform size as Eq. (44).

From the above analysis, it is obvious that if a particular problem is known to contain only small angle propagation, the mesh size $(\Delta r, \Delta z)$ may be increased and, subsequently, the run-time will be reduced. Conversely, for problems where very large angle propagation is expected to be important a small mesh size may be required. To allow for the highest angles of propagation in typical environments, we set $\theta_{max} \approx \theta_{critical} \approx 30^\circ$ in Eqs. (44) through (46) and obtain

$$\Delta z_{max} \sim 2\lambda \tag{47}$$

and

$$\Delta r_{max} \sim 4\lambda \quad . \tag{48}$$

In other words, accurate solutions should be obtained when both Δr and Δz are on the order of a few acoustic wavelengths. Note that this mesh size is considerably larger than that needed by other numerical algorithms based on finite difference or finite element approximations to the differential operators in range-dependent environments. As this analysis will show, smaller grid sizes, on the order of a wavelength in range and a fraction of a wavelength in depth, are required to achieve optimal accuracy in shallow water environments with strong bottom interactions.

MMPE Boundary Conditions

The MMPE model treats the surface as a perfect reflector due to a pressure release boundary. This is a Dirichlet boundary condition defined by

$$\psi(z = 0) = 0 \quad . \tag{49}$$

A popular technique used in PE/SSF models to achieve this is the image ocean method. With this method, we assume an identical image ocean overlays the real ocean for negative values of depth and, furthermore, the acoustic field is exactly equal but of opposite sign in the image ocean, i.e.

$$\psi(-z) = -\psi(z) \quad . \tag{50}$$

The boundary condition (49) is then satisfied automatically.

In our numerical implementation, therefore, we must define our field array to be twice as long (i.e., twice as deep) as necessary to describe the real and image acoustic field. Within each range step, the MMPE model assures this symmetry by simply imposing condition (50) on the image field for $z < 0$ after multiplying by the z-space operator in the real ocean (thus removing the need to actually define the image environment). This formulation allows direct implementation of the split-step Fourier algorithm given by Eq. (35) using the full FFT transformations from z-space to k_z-space.

The MMPE model treats the bottom as a fluid of contrasting sound speed and density from that of water. In addition, the MMPE model allows for an additional bottom layer to exist on top of the basement to allow for effects of sediment layers to be included. Within either bottom

volume, the PE environmental potential function, $U_{op}(z)$, is defined as before in terms of the local acoustic index of refraction, $n(z) = \frac{c_0}{c(z)}$, where $c(z)$ now includes the sound speed within the bottom volume. The effect of approximating the bottom as a fluid is the neglect of shear wave propagation. When the true bottom does support shear waves, the conversion of compressional energy incident on the interface into downward propagating shear energy is treated as a loss. In this manner, the bottom properties are replaced by equivalent fluid properties that produce the correct reflection from the interface. This is discussed further at the end of this section.

We assume the interface between the bottom of the water column and the top of the basement, or sediment, layer is characterized by a sharp contrast in sound speed. In a numerical code with finite sampling and recurrent use of FFT's, it is desirable to use smoothly varying, continuous functions to avoid artificial reflections, aliasing, and noise from entering into the calculation. Therefore, we seek to find a smooth, continuous function of variable scale which can accurately reproduce the physical effects of a discontinuous jump in sound speed at the water/ bottom interface.

We write the interface condition for the sound speed as

$$c(z) = c_w(z) + [c_b(z) - c_w(z)]H(z - z_b) \tag{51}$$

where we shall assume that the sound speed above the interface at $z = z_b$ has a constant value of c_w and below the interface has a value c_b. The Heaviside step function is defined by

$$H(\zeta) = \begin{cases} 0, & \zeta < 0 \\ \frac{1}{2}, & \zeta = 0 \\ 1, & \zeta > 0 \end{cases} \tag{52}$$

where $\zeta \equiv z - z_b$. From the theory of generalized functions,[17] we may replace $H(\zeta)$ by any smooth function within a class of generalized functions that produces the same overall effect (i.e., has similar moments).

One such function satisfying the above criteria involves the hyperbolic tangent function,

$$\overline{H}(\zeta) = \frac{1}{2}\left[1 + \tanh\left(\frac{\zeta}{2L_c}\right)\right] \tag{53}$$

or, equivalently,

$$\overline{H}(\zeta) = (1 + e^{-\zeta/L_c})^{-1} \quad . \tag{54}$$

This function has the properties

$$\bar{H}(\zeta) \to 0, \quad \zeta \ll 0; \tag{55}$$

$$\bar{H}(\zeta) = \frac{1}{2}, \quad \zeta = 0; \tag{56}$$

and

$$\bar{H}(\zeta) \to 1, \quad \zeta \gg 0 \, . \tag{57}$$

Furthermore, the derivative of the Heaviside function is

$$H'(\zeta) = \delta(\zeta) \tag{58}$$

where $\delta(\zeta)$ is the Dirac-delta function and is characterized by

$$\int_{-\infty}^{\infty} \delta(\zeta) d\zeta = 1 \, . \tag{59}$$

Similarly, the derivative of $\bar{H}(\zeta)$ is

$$\bar{H}'(\zeta) = \bar{\delta}(\zeta) = \frac{1}{4L_c} \operatorname{sech}^2\left(\frac{\zeta}{2L_c}\right) \tag{60}$$

and it is easy to show that

$$\int_{-\infty}^{\infty} \bar{\delta}(\zeta) d\zeta = 1 \tag{61}$$

is also satisfied. This mixing function $\bar{H}(\zeta)$ is parameterized by a characteristic mixing length, L_c. It is obvious from the above analysis that

$$\lim_{L_c \to 0} \bar{H}(\zeta) = H(\zeta) \tag{62}$$

and

$$\lim_{L_c \to 0} \bar{\delta}(\zeta) = \delta(\zeta) \, . \tag{63}$$

This limiting equality can be shown to hold for higher derivatives as well.

We have now introduced an additional parameter into our model, the sound speed mixing length, L_c. This can be adjusted by the user in an attempt to create the most realistic interface condition for reflections from a sound speed discontinuity. The MMPE code then employs Eq. (54) to mix the sound speed profiles above and below the interface (or interfaces) at $z = z_b$. Experience has shown that the most accurate results are gained by defining L_c as a fraction of an acoustic wavelength, specifically, $\lambda/10$. However, in order to maintain a smooth shape and proper sampling of the PE potential function $U_{op}(z)$, a default minimum value for L_c has been set at $L_{c\min} = \Delta z$. This suggests that the most accurate solutions are obtained when the depth mesh Δz is less than a wavelength. Thus, one should look for convergence of the solution as the depth mesh is decreased.

The effect of density on acoustic propagation has not yet been considered. In fact, the variation of density was ignored in the original form of the Helmholtz equation. In a fluid with a variable density ρ, one can easily show that the previous form of the Helmholtz equation, Eq. (3) or (6), can be obtained if the index of refraction n is replaced by an "effective" index of refraction given by

$$n'^2 = n^2 + \frac{1}{2k_0^2}\left[\frac{1}{\rho}\nabla^2\rho - \frac{3}{2}\left(\frac{1}{\rho}\nabla\rho\right)^2\right] . \tag{64}$$

Solutions for the pressure field $p(r, z)$, now defined by

$$p(r, z) = P_0\sqrt{\frac{\rho R_0}{\rho_0 r}}Q_{op}^{-1/2}\psi(r, z)e^{ik_0 r} , \tag{65}$$

may be obtained by marching the solution of the PE function $\psi(r, z)$ out in range with the definition

$$U_{op}(z) = U_1(z) + U_2(z) \tag{66}$$

where $U_1(z)$ is the same environmental potential function previously defined and $U_2(z)$ accounts for the effect of the density discontinuity. Note that a reference density, $\rho_0 = 1.0$ g/cm^3, has been introduced to keep the leading factor in Eq. (65) dimensionless.

If we assume that $\rho = \rho(z)$ only, then the density is defined by

$$\rho(z) = \rho_w + (\rho_b - \rho_w)H(z - z_b) \tag{67}$$

where $H(\zeta)$ is the Heaviside step function described previously, and ρ_w and ρ_b are the densities (assumed constant) of the water column and bottom sediment, respectively. Obviously, the function $U_2(z)$ is non-zero only in the vicinity of the interface. As before, we wish to spread this discontinuity over some finite region in terms of smooth generalized functions. This is a more critical problem than before because $U_2(z)$ depends not on the density but on the derivatives of the density. As before, it is necessary to define a mixing function, with its subsequent derivatives, to describe the interface condition. However, this introduces a density mixing length L_ρ, the choice of which has always been somewhat ambiguous in this definition.

Tappert[18] has shown that a good approximation for $U_2(z)$ is

$$U_2(z) \approx -\frac{\varepsilon}{k_0^2} \frac{\partial^2}{\partial z^2} H(z - z_b) \tag{68}$$

where

$$\varepsilon = \left[\frac{1 - (\rho_w / \rho_b)^{1/2}}{1 + (\rho_w / \rho_b)^{1/2}} \right] . \tag{69}$$

For small density contrasts, this is equivalent to neglecting the last term in Eq. (64). The main argument used to justify this approximation is that because we are using generalized functions to represent the density discontinuity, the function $U_2(z)$ must also be defined in terms of generalized functions. However, the last term in (64) contains the square of a generalized function, specifically $\bar{\delta}^2(z')$, which is not a generalized function. This detailed analysis by Tappert, which attempted to remove as much singularity as possible from the solution in the vicinity of the density discontinuity, showed that Eq. (68) is the best expression to use. Furthermore, this formulation inherently produces the best results when L_ρ is minimized, i.e. as $L_\rho \to 0$. Note that L_ρ must still be large enough such that the finite depth mesh adequately samples the function $U_2(z)$ (which is not a simple jump as U_1 was).

For purposes of defining a mixing function which completely localizes the extent of the function to within a finite distance from the interface, we choose a cubic spline over the finite interval $-L_\rho \le \zeta \le L_\rho$. In designing a cubic spline approximation for $H(\zeta)$, we have used four sub-intervals of length $L_\rho/2$. Requiring continuity of the function and its first and second derivatives, we define

$$\bar{H}(\zeta) = \begin{cases} 0 & , \quad \zeta \le -L_\rho \\ \frac{2}{3}\left(1+\frac{\zeta}{L_\rho}\right)^3 & , \quad -L_\rho \le \zeta \le -\frac{L_\rho}{2} \\ \frac{1}{2}+\frac{\zeta}{L_\rho}-\frac{2}{3}\left(\frac{\zeta}{L_\rho}\right)^3 & , \quad -\frac{L_\rho}{2} \le \zeta \le \frac{L_\rho}{2} \\ 1-\frac{2}{3}\left(1-\frac{\zeta}{L_\rho}\right)^3 & , \quad \frac{L_\rho}{2} \le \zeta \le L_\rho \\ 1 & , \quad \zeta \ge L_\rho \end{cases} . \tag{70}$$

The first derivative of this function is then

$$\bar{H}'(\zeta) = \bar{\delta}(\zeta) = \begin{cases} 0 & , \quad \zeta \le -L_\rho \\ \frac{2}{L_\rho}\left(1+\frac{\zeta}{L_\rho}\right)^2 & , \quad -L_\rho \le \zeta \le -\frac{L_\rho}{2} \\ \frac{1}{L_\rho}\left[1-2\left(\frac{\zeta}{L_\rho}\right)^2\right] & , \quad -\frac{L_\rho}{2} \le \zeta \le \frac{L_\rho}{2} \\ \frac{2}{L_\rho}\left(1-\frac{\zeta}{L_\rho}\right)^2 & , \quad \frac{L_\rho}{2} \le \zeta \le L_\rho \\ 0 & , \quad \zeta \ge L_\rho \end{cases} . \tag{71}$$

Note that $\bar{\delta}\left(-\frac{L_\rho}{2}\right) = \bar{\delta}\left(\frac{L_\rho}{2}\right) = \frac{1}{2L_\rho}$ and $\bar{\delta}(0) = \frac{1}{L_\rho}$, so it is obvious that

$$\int_{-\infty}^{\infty} \bar{\delta}(\zeta)\,d\zeta = 1 \tag{72}$$

and, therefore,

$$\lim_{L_\rho \to 0} \bar{\delta}(\zeta) = \delta(\zeta) \tag{73}$$

as required.

Finally, the second derivative is

$$\bar{H}''(\zeta) = \bar{\delta}'(\zeta) = \begin{cases} 0 & , \quad \zeta \le L_\rho \\ \frac{4}{L_\rho^2}\left(1 + \frac{\zeta}{L_\rho}\right) & , \quad -L_\rho \le \zeta \le -\frac{L_\rho}{2} \\ -\frac{4}{L_\rho^2}\left(\frac{\zeta}{L_\rho}\right) & , \quad -\frac{L_\rho}{2} \le \zeta \le \frac{L_\rho}{2} \\ -\frac{4}{L_\rho^2}\left(1 - \frac{\zeta}{L_\rho}\right) & , \quad \frac{L_\rho}{2} \le \zeta \le L_\rho \\ 0 & , \quad \zeta \ge L_\rho \end{cases} . \tag{74}$$

Combining (74) with (68) gives the formula for computing the density potential function by employing a cubic spline polynomial smoothing function.

As before, we define a lower limit default of $L_{\rho\min} = 2\Delta z$, and when this limit is reached the mixing function is centered on the mesh nearest the true interface depth. Smaller values than this will not properly sample the mixing function. Analysis has shown that accurate solutions can be obtained by applying the condition $L_\rho \sim 2\lambda$, which yields the condition $\Delta z_{\max} \sim \lambda$. This is a stronger condition than before and suggests that twice the former transform size is needed to utilize the mixing function. However, because of the finite nature of this representation, this condition may be relaxed slightly. A good rule of thumb for either mixing function is $\Delta z_{\max} \sim \lambda$ when sound speed and density discontinuities are important for computing the correct reflection from the interface. Again, tests for convergence should be applied.

Finally, this author would like to note that it is this treatment of the bottom interface which remains the weak point of this model. In deep ocean problems, where bottom interactions are less significant, this model has been quite effective.[19] However, with the current emphasis on shallow water propagation, more work needs to be done to improve this treatment of the bottom boundary condition and to understand the implications of generating such mixing functions. At the present time, this is the only method for dealing with the bottom interface within the context of the SSF algorithm. Other investigators have also developed a successful hybrid SSF/finite-difference approach to solve for the density term in the effective index of refraction.[20] But other potential treatments should be investigated.

MMPE Source Function

We now define the initial conditions for the PE field function, $\psi(r = 0, z)$. Previously, we have assumed the relationship between ψ and the acoustic pressure, ignoring the effect of density and the WKBJ factor, is of the form

$$p = P_0\sqrt{\frac{R_0}{r}}\psi e^{ik_0 r} . \tag{75}$$

We obviously cannot define p at range $r = 0$ from this expression. This is analogous to the undefined amplitude of a point source Green's function at the source location. Therefore, we choose to define the source amplitude relative to that at some small but finite distance from the source. Specifically, we choose

$$p(r = R_0) = P_0 \ . \tag{76}$$

Consistent with reference values used in most sonar equations, we define the reference range

$$R_0 = 1 \text{ m} \tag{77}$$

and the source level, *SL*, is related to P_0 by

$$SL = 20\log\left(\frac{P_0}{P_r}\right) \text{ dB re } P_r R_0 \ . \tag{78}$$

The dB units of *SL* are explicitly stated relative to a reference pressure value of $P_r = 1\ \mu\text{Pa}$ at the reference range R_0.

We are still left with the task of determining a form for the source field $\psi(r = 0, z)$. We begin by writing Eq. (75) as

$$\psi(r, z)e^{ik_0 r} = \frac{1}{P_0}\sqrt{\frac{r}{R_0}}p(r, z) \tag{79}$$

from which it follows that

$$\psi(r = 0, z) = \lim_{r \to 0}\frac{1}{P_0}\sqrt{\frac{r}{R_0}}p(r, z) \ . \tag{80}$$

In the vicinity of a point source, we know the pressure field takes the form of the spherical Green's function. Thus, we write

$$p = \frac{a}{4\pi R}e^{ik_0 R} \ , \ R = \sqrt{r^2 + z^2} \ , \ a = P_0 R_0 \tag{81}$$

where a is defined by requiring $|p| = \frac{P_0}{4\pi}$ at $R = R_0$. We represent the source at $(0, z_S)$ as a point source by defining

$$\psi(r = 0, z) = \alpha\delta(z - z_S) \ , \tag{82}$$

where α is a normalization factor. Integrating both sides of Eq. (80) over all (real) depths, and taking the far-field approximation, yields

$$\alpha = \sqrt{\frac{iR_0}{2\pi k_0}} \ . \tag{83}$$

It is desirable to begin the calculation by specifying the source in the *k*-domain. Including the influence of the image source, a straightforward Fourier transform of Eq. (82) yields

$$\hat{\psi}(r = 0, k) = \alpha \int_{-\infty}^{\infty} [\delta(z - z_S) - \delta(z + z_S)] e^{-ik_z z} dz = -2i\alpha \sin(k_z z_S) \ . \tag{84}$$

which indicates that the wavenumber representation of the starting field has a constant amplitude modulated by a phase due to the interaction of the source and its image. This constant amplitude is consistent with the notion of an omnidirectional point source which puts equal energy into all wavenumbers (i.e., all directions).

For the wide angle PE approximations, it is tempting to allow the amplitude of this function to be unity for all wavenumbers, thereby equally populating all directions of propagation. However, even the wide angle approximations are assumed valid only up to angles of 40° or so. Additionally, the finite FFT size will restrict how large k_z / k_0 can be. Therefore, a smooth taper is included at high absolute wavenumber values to limit the angular width of the source function and to reduce the influence of sidelobes. Thomson and Bohun[21] have also shown that a wide angle source needs to be modified by the factor

$$F(k_z) = \left(1 - \frac{k_z^2}{k_0^2}\right)^{-1/4} \ , \ (|k_z| < k_0) \tag{85}$$

to produce the correct solution in the far-field. This results from proper treatment of the WKBJ factor in the definition of the starting field. Note that $k_z = k_0$ corresponds to $\theta = 90^\circ$, so $|k_z| > k_0$ represents imaginary angles of propagation (evanescent modes). It is required then that the source function be tapered within the limits of $\left|\frac{k_z}{k_0}\right| < 1$.

Note that in order to accommodate the so-called "1/2 mesh symmetry" as defined by the depth gridding given in Eq. (40), it is also necessary to add a phase term in the wavenumber domain of $e^{ik_z \frac{\Delta z}{2}}$. Thus, the final form for the wavenumber domain starting field for the wide angle point source is now given by

$$\hat{\psi}(r = 0, k_z) = -2i\sqrt{\frac{iR_0}{2\pi k_0}}\sin(k_z z_S)\left(1 - \frac{k_z^2}{k_0^2}\right)^{-1/4} e^{ik_z\frac{\Delta z}{2}} \quad . \tag{86}$$

Other MMPE Implementation Tricks

There remain numerous other tricks within the MMPE model which should be noted. Volume attenuation within the water column and sediment layers, $\alpha(z)$, is treated simply by damping the solution in the *z*-domain by the factor

$$e^{-ik_0\Delta r U_{loss}(z)} = e^{-\Delta r\alpha(z)} \tag{87}$$

which defines the introduction of an additional term in the *z*-space propagator function,

$$U_{loss}(z) = -\frac{i}{k_0}\alpha(z) \quad . \tag{88}$$

In terms of transmission loss, this reduces the field by

$$TL_\alpha = -20\log(e^{-\Delta r\alpha}) = 8.686\Delta r\alpha \text{ dB} \; . \tag{89}$$

The MMPE model assumes values input for volume attenuation have units [dB/m/kHz]. Internally, these values are multiplied by the frequency of the calculation (in kHz) which produces values equivalent to 8.686α. These can then be used to define the loss function given in Eq. (88). Empirical expressions for the volume attenuation in sea water are generally used in the model, but were removed from the calculations for the SWAM'99 test cases which assumed no loss in the water column.

As mentioned previously, the treatment of shear within the MMPE model is simply in terms of defining an equivalent fluid bottom. Both the compressional attenuation and density are given effective values based on the analysis of Tindle and Zhang.[22] This provides a reasonable approximation to both the phase and amplitude of the reflection coefficient for low grazing angles. Specifically, a bottom with compressional and shear speeds c_b and c_s, respectively, density ρ_b and compressional and shear attenuations α_b and α_s, respectively, can be represented by an equivalent fluid bottom with compressional speed c_b, effective density

$$\rho_b' = \rho_b\left(1 - 2\frac{c_s^2}{c_b^2}\right) \tag{90}$$

and effective attenuation

$$\alpha_b' = \alpha_b + \frac{4c_s^3(c_b^2 - c_w^2)}{c_b(c_w^2 - 2c_s^2)^2}\left[2\alpha_s + \frac{\omega(c_b^2 - c_w^2)^{1/2}(c_w^2 - c_s^2)^{1/2}}{c_b c_w^2}\right] . \quad (91)$$

Note that Eq. (91) requires that $c_s < c_w < c_b$. In cases where $c_w > c_b$, it is unrealistic to expect anything but very small shear speed values, and so they are assumed to be zero in such cases. These formulae are implemented in the MMPE model at each interface with the understanding that the upper layer is treated as the fluid and the lower layer is treated as the solid. A more recent analysis of the parameters of an equivalent fluid bottom by Zhang and Tindle[23] showed an improvement over this method by defining a complex effective density. This treatment works better at higher shear speed values and higher grazing angles. The necessary equations are currently being implemented into the MMPE model and should be available by the time of publication of this paper. However, during the SWAM'99 Workshop, it was apparent that the introduction of shear into some of the environments had negligible effect. Therefore, the treatment of shear will not be analyzed in this paper.

The way in which environmental inputs are treated should also be noted. Within the MMPE model, every input sound speed profile is first run though a simple interpolation routine to define the value of the sound speed on the grid points in depth. This interpolated profile is then smoothed by using a simple 1-2-1 smoothing routine. This is to wash out any unrealistic "kinks" in the sound speed profile interpolation which may result in numerical scattering. Then, at each range step, a linear interpolation between these smoothed sound speed profiles at each grid point in depth is performed. This is done even at depths greater than the bottom depth. Only after this final interpolated sound speed profile is created is it combined, via the previously defined mixing functions, with the bottom sound speed profile. Note that the bottom profile, which could be left equally as general as the water column, is simply defined by a value at the interface and a constant gradient within the sediment. Naturally, this treatment of the environment will not have any impact on the results generated for the isospeed water column test cases.

This combination of the water column sound speed and bottom sound speed, as well as the density mixing function, are defined at the depth of the bottom interface. This bathymetry data is also input in a range-dependent manner, and bottom depths at intermediate ranges are defined by a simple linear interpolation between given range points. Note that the bottom interface depth need not fall exactly on a grid point since the mixing functions generally extend over several grid points in depth. The center of these mixing functions is, by definition, at the given bottom interface depth. Thus, more accurate solutions may require smaller mesh sizes in depth to better characterize the true location of the bottom interface.

Another set of implementation tactics employed in the MMPE model relates to undefined filters, or "sponges", employed to remove acoustic energy from very deep depths in the bottom (from which no energy is expected to return) and from very high angles of propagation. The most obvious need for a filter we first recognize is the radiation condition $\psi(z) \to 0$ as $z \to \pm\infty$. Because the computational depth is finite, however, we must force the field amplitude to zero at the maximum depth. Note this also serves to eliminate wrap-around between the real and image

oceans. This must be done in a smooth and relatively "slow" manner to avoid reflections from the filter function itself. The MMPE model applies a sine-squared filter function to the bottom third of the computational depth of the real ocean. Because there is no energy at these depths at the initial range, it is not necessary to create a filter which goes from unity all the way down to zero. Rather, since this filter is applied at every range step anyway, it is only necessary to reduce the field by some fractional amount at the deepest depths. After multiple applications of such a filter, the deepest part of the signal will be greatly reduced. Thus, the sine-squared filter is designed to range from unity down to only 0.5. Without reducing the level completely to zero in a single step, this has the advantage of reducing the numerical reflections often caused by this filter function.

Similarly, some type of filtering may be needed in the k_z-domain to remove angles beyond $90°$, i.e. $k_z > k_0$. As previously noted, the form of the wavenumber domain propagator function, defined in Eq. (36), naturally provides a filter for these angles by making them evanescent. Thus, energy is attenuated beyond this limit, assuming the k_z-space is sampled at such high values. If, on the other hand, the FFT size N is smaller such that $k_{z,\,max} < k_0$, a k_z-domain filter is needed to avoid numerical reflections at $k_{z,\,max}$. An identical filter as that used in the z-domain is employed for that purpose.

III. Convergence and Stability Issues

In this section, we apply the previously defined PE/SSF algorithm to the first flat-bottom test case of the SWAM'99 environments. We will limit our analysis here to the 250 Hz CW source at a depth of 30 m. A schematic of the environment is provided below in Fig. 1. This environment has an isospeed water column overlying a flat bottom. The bottom properties are defined every 2 km and, as described in the previous section, these are linearly interpolated in range out to 20 km. There is no shear in the bottom, and the compressional attenuation is fixed at 0.1 dB/λ. The remaining bottom properties defined, sound speed, sound speed gradient, and density, are also displayed in Fig. 1 to provide some idea of the level of variability in the bottom.

Figure 2 displays the full, CW field at 250 Hz for the source at 30 m, including the $1/\sqrt{r}$ cylindrical spreading loss. It also shows the TL trace at a receiver depth of 35 m out to a range of 20 km. This calculation was performed with an FFT size of N = 4096 and a computational depth of z_{max} = 400 m, corresponding to a depth mesh size of about 0.2 m (including the image ocean). At 250 Hz, this provides a depth sampling of roughly 0.03λ. The range step size was chosen to be Δr = 5 m, on the order of a wavelength. These values were found to produce the best curve, as will be shown in more detail below. It should be noted that all calculations were made on a 500 MHz Pentium based PC. For these values of the calculation parameters, this single frequency run took approximately 1 minute to complete.

Reciprocity

First, let us examine this result under the context of the reciprocity test. As stated previously, if an identical point source is placed in the environment at the 20 km range at a depth of 35 m, and the field propagating through the reciprocal (range-reversed) environment is computed, then the solution back at the original source location should be the same. Specifically,

$$p_f(r = 20 \text{ km}, z = 35 \text{ m}) = p_r(r = 0 \text{ km}, z = 30 \text{ m}) \quad (92)$$

where p_f is the "forward propagating" field due to a point source at $r_s = 0$ km, $z_s = 30$ m and p_r is the "reciprocal propagating" field due to a point source at $r_s = 20$ km, $z_s = 35$ m. The results of such a reciprocity test are displayed in Fig. 3, where it is observed that reciprocity is obeyed to within less than a tenth of a dB in transmission loss (less than a 1% error in amplitude) and less than two-tenths of a degree in phase.

In fact, the accuracy used in the depth mesh was not necessary to achieve this level of confirmation of reciprocity. Smaller FFT sizes in the PE/SSF algorithm can still produce reciprocal results, even though the solution may have not yet converged. Thus, it is important to recognize that, although this reciprocity test is a necessary one to evaluate the validity of the model, it is not sufficient to guarantee an accurate solution.

Convergence

We shall now focus on the issues relating to convergence, and thereby examine in detail the structure of the solution and the propagators employed in the calculation. As the baseline calculation, we shall consider the parameters stated previously, an FFT size of $N = 4096$, a computational depth of $z_{max} = 400$ m, and a range step size of $\Delta r = 5$ m. Figure 4 compares the TL trace at a receiver depth of 35 m for various values of N, the FFT size. Note that the range has been expanded to enhance the first and last 5 km of the run.

These results suggest that convergence has essentially been reached at an FFT size of $N = 4096$. This is a bit misleading, though, and should be clarified. The real reason the $N = 1024$ data does not match up as well as the other curves is because of the mixing lengths at the bottom interface. Specifically, for $N = 1024$, the depth mesh is $\Delta z = 0.78125 \text{ m} \approx 0.13\lambda$. Thus, the minimum sound speed mixing length condition $L_{c\min} = \Delta z$ just exceeds the optimal value of $L_c = \lambda/10$. For all higher values of N, the latter value is used. Upon closer inspection, we find that values higher than $N = 4096$ do produce slightly different results. However, these differences are less than a dB in level and, at very high values of N, begin to introduce numerical noise in the SSF algorithm.

Just from this analysis, we are already confronted with a convergence issue. If we relaxed the condition on the optimal sound speed mixing length to $L_c \sim \lambda$, we would find *general* convergence in the solution at smaller values of N, around 256. This corresponds to a depth mesh of $\Delta z = 3.125 \text{ m} \approx 0.5\lambda$. Higher values of N would be found to change the solution slightly, but only due to more accurate interpolation between grid points to the desired depth of 35 m. This is consistent with the use of FFT's in the algorithm, i.e. sampling smaller than $\lambda/2$ does not provide any real additional information, and so does not improve the general solution.

Since the model defines $L_c = \max(\Delta z, \lambda/10)$, this is a crucially important point. General convergence will not be obtained until $\Delta z \le \lambda/10$, requiring larger values of N and

longer run times. For the current calculation, with the range step fixed at $\Delta r = 5$ m, the run time for $N = 4096$ is roughly 1 minute as compared to $N = 256$ which completes the calculation in under 3 seconds. The significance of this difference is even more obvious when one begins to consider broadband calculations which scale linearly with the number of frequencies computed.

So why define $L_c = \max(\Delta z, \lambda/10)$ rather than $L_c = \max(\Delta z, \lambda)$? To address this issue, we set $N = 4096$ and vary the size of L_c relative to λ. (L_ρ is fixed at 2λ.) Figure 5 displays the results for several values of L_c. The upper two panels display the TL trace at 35 m for the first and last 5 km of the calculation, as before. However, in this case, there is no clear convergence near the final ranges. All four values of L_c produce slightly variable results. Thus, it is not clear that convergence is even possible due to this ambiguity in the sound speed mixing length. As a means of determining which value is "best", the third panel of Fig. 5 displays only the first 2 km of the calculation. There, we see that the results do appear to converge for $L_c \sim \lambda/10$. Note that discrepancies begin at roughly 0.5 km. This is presumably due to the interaction of low modes which are more sensitive to this choice of mixing length. Other fractional wavelength values were chosen, and $L_c \sim \lambda/10$ consistently seemed to provide the best convergence.

Fixing the sound speed mixing length at $L_c \sim \lambda/10$ and $N = 4096$, we now examine the convergence with respect to the density mixing length. The results are displayed in Fig. 6. It is clear from this figure that there is a limit to how small this mixing length can be to produce accurate results. It is unclear whether this is merely a numerical issue, a problem with the form of the mixing function, or whether it is something more fundamental in the approximate form of the density treatment as defined in Eq. (68).

For the three larger values of density mixing length used, the middle panel shows a considerable amount of variability in solutions with no clear convergence occurring. Again, we focus our attention on the lower panel where the results of the first 2 km of the calculation are displayed. It appears that a "stable" solution begins to appear when $L_\rho \sim 2\lambda$. The term "stable" rather than "convergent" is used since this is not a limiting effect as L_ρ is increased or decreased indefinitely. For values of L_ρ much greater or less than this, the solution appears to degrade, as seen in the middle panel for $L_\rho = \lambda/5$.

We now consider the final free parameter, the range step size Δr. As noted previously, the algorithm is based on the centered-step scheme which is third order accurate in Δr. This implies that as the range step is continually decreased, the solution should continue to improve in accuracy until it converges to a stable solution. This is true in most PE models, including those based on implicit finite difference or finite element methods. However, this is not the case when the SSF algorithm is employed.

In Figs. 7 and 8, the solutions are displayed for several different values of range step size. The solution appears to be converging in Fig. 7 at $\Delta r \sim 5$ m. The smaller value of $\Delta r = 2$ m does not significantly change the solution. We would expect that even smaller values would also

not change the solution. However, as observed in Fig. 8, this does not hold true. The solution is seen to degrade for smaller values of Δr. Thus, the solution does not converge with decreasing Δr but rather reaches a stable solution at finite Δr. From this analysis, it appears that the solution reaches such a stable solution at $\Delta r \sim \lambda$. Note, as is often one of the stated advantages of the PE/SSF model, the range step can be several wavelengths and still achieve accurate solutions at shorter ranges. For longer ranges, it appears that a range step on the order of a wavelength may be necessary.

But what is the cause of this non-convergence at small range steps? This is a little known feature of the SSF algorithm, and is related to the structure of the propagator functions. For the same range step sizes used above, the environmental propagator function, $e^{-ik_0 \Delta r U_{op}(r,z)}$, where $U_{op}(r,z)$ is given by Eq. (25), is displayed in Figs. 9 and 10. The corresponding wavenumber propagator function, $e^{-ik_0 \Delta r \hat{T}_{op}(k_z)}$, where $\hat{T}_{op}(k_z)$ is given by Eq. (36), is displayed in Figs. 11 and 12. Note that the magnitude of the environmental propagator exhibits the decay of the solution at deep depths down to 0.5, and the wavenumber propagator decays exponentially beyond $k_z > k_0$.

Based on the previous conclusion that a range step of $\Delta r \sim 5$ m provided the most stable solution, the shapes of the propagator functions suggest the following. For large Δr, the SSF algorithm attempts to put a lot of phase information into a single range step. If Δr is too large, this generates errors in the solution. On the other hand, for small Δr, there is little phase information in each range step. And if Δr is too small, there is not enough phase information to produce a stable, accurate solution. Also note that, for small Δr, the exponential decay of high wavenumbers beyond $k_z > k_0$ does not occur as effectively, and such non-realistic energy may creep into the solution as noise.

The general conclusion we may draw from this analysis of the propagator shapes is that stable, accurate solutions occur at range steps where there is a full cycle of phase information in each propagator. This appears to occur when $\Delta r \sim \lambda$ in this shallow water environment. Solutions close to this stable solution may also be obtained using range steps of a few wavelengths, particularly in deeper water or at shorter ranges.

In this section, we have clearly seen the difficulty in obtaining convergent, accurate solutions with the SSF/PE model. However, for the remainder of this section, we shall fix the free parameters, unless otherwise noted, as $\Delta r \sim \lambda$, $\Delta z < \lambda/10$, $L_c = \max(\Delta z, \lambda/10)$, and $L_\rho = \max(5\Delta z, 2\lambda)$. The latter two conditions defining the mixing lengths are explicitly written into the MMPE model, and Δr and Δz will be adjusted depending on the frequency and depth of the problem.

Comparison With Other Solutions

Based on the previous analysis of the FLATa environment at 250 Hz, the best solution is obtained when a range step of $\Delta r = 5$ m and an FFT size of $N = 4096$ are used. To check the

true accuracy of this calculation requires a benchmark solution. However, no formal benchmark solutions were generated for the SWAM'99 test cases. This was intentional so that each different model's results could be compared for consistency or differences without the aid of a true solution to guide the modeler. Fortunately, there were two different models, those developed by Brooke, *et al*.[24] and Mikhin[25] which showed excellent agreement for several test cases. Thus, for the purposes of benchmarking, we shall assume that these results represent the "true" solutions.

Figure 13 displays the results from Dmitry Mikhin's model and the MMPE model for the FLATa case at 250 Hz for a source depth at 30 m and a receiver trace at 35 m. In this figure, the MMPE model used values of $\Delta r = 5$ m and $N = 4096$. The maximum computational depth was $z_{max} = 400$ m, so the depth mesh size was $\Delta z = (2z_{max})/N \approx 0.03\lambda$. The comparison is reasonably good, in this author's opinion. The larger scale structures, fluctuating with range scales of ~ 0.5 km, appear to agree throughout most of the range. It should also be noted that the agreement is quite good for ranges less than 2 km. Still, one may argue that the MMPE solutions seem to contain more numerical noise. The differences at longer ranges may simply be due to the treatment of the bottom interface for which the MMPE model has introduced the mixing functions previously described. A proper test of the accuracy of the MMPE model may then require a solution of this modified environment. However, the purpose of this exercise is to determine the model's ability to generate solutions to the prescribed environment, and these differences should be accepted as limitations of the current technique.

During the course of our convergence/stability analysis, we observed that larger FFT sizes appeared to reach convergent solutions, although very large FFT sizes introduced some small scale numerical noise. Thus, we may expect this to be partly to blame for this effect. To test this, we should reduce the FFT size. However, because of our condition on sound speed mixing length, $L_c = \max(\Delta z, \lambda/10)$, increasing Δz beyond $\lambda/10$ will begin to degrade the solution. So as a limiting case, we now choose $N = 1024$ which corresponds to $\Delta z \approx 0.13\lambda$, approximately matching the limiting value allowed for L_c. The comparison of these results with the converged solution of Mikhin's is displayed in Fig. 14.

The results are seen to improve noticeably at all ranges, particularly with the removal of some of the small-scale numerical noise. This is also advantageous because it reduces the run-time of the calculation from roughly one minute down to about 12 seconds, nearly a factor of six improvement. Thus, it appears that the MMPE generates the most accurate and efficient solution when $\Delta r \sim \lambda$ and $\Delta z \sim \lambda/10$. These conditions will be used throughout most of the remainder of this paper to produce the most accurate MMPE solutions.

Finally, before we accept that this resolution is needed in general, let us examine one more solution when we relax our grid conditions to $\Delta r \sim \lambda$ and $\Delta z \sim \lambda/2$. For the current environment, that means reducing the FFT size to $N = 256$. Note that this run can be completed in roughly 3 seconds. The comparison of the results with Mikhin's solution is given in Fig. 15. Obviously, the accuracy of the solution has been severely degraded at larger ranges. However, the results are still quite good at ranges less than about a km, or roughly 10 water depths. This is likely a characteristic feature of the PE/SSF solution in shallow water: for ranges less than ~ 10

water depths, a depth mesh of $\Delta z \sim \lambda/2$ is adequate, but for longer ranges, finer sampling in depth is needed down to our limit of $\Delta z \sim \lambda/10$.

IV. SWAM'99 Test Case Results

Based on our analysis of the MMPE model solutions for the FLATa environment at 250 Hz, we can now examine the accuracy of the model using a generalized approach. In most of the following cases, the MMPE solutions have been generated using $\Delta r \sim \lambda$ and $\Delta z \sim \lambda/10$. Exceptions to this are noted. The CW results are again compared with Mikhin's solutions.

FLATa

In Fig. 16, the results for the FLATa environment are presented for a 25 Hz source at 30 m and a receiver trace at 35 m. For this low frequency, it was found that a smaller depth mesh was necessary to achieve the best result, specifically, $\Delta z \sim \lambda/20$. The difficulty with this problem was apparently the scale of the wavelength, 60 m, compared to the scale of the waveguide, 100 m. Thus, this density mixing length, 2λ, is actually larger than the waveguide itself! In light of this, it is rather remarkable that the solution compares as well as it does. However, it does appear that the MMPE model is not well suited for very low frequency propagation in shallow water where only a few propagating modes exist.

The solution for the 500 Hz source is shown in Fig. 17. The level of accuracy of these results is comparable to the 250 Hz solutions examined in the previous section. The fine-scale structure matches well for the first few km while the larger scale features match well at all ranges. One may expect that a comparison of range-averaged solutions would agree extremely well at all ranges.

Finally, the 1000 Hz solutions are compared in Fig. 18. Again, we find the fine-scale features agree well at shorter ranges while the general structure is consistent at all ranges. Similar comparisons were consistently found for all of the FLAT environments, and will not be discussed further. For the remainder of this section, only the 250 Hz and 500 Hz solutions will be analyzed.

DOWNa

This environment combines bottom acoustic parameter variability with a variable downslope bathymetry, increasing the bottom depth from 50 m at the source range to over 200 m at 20 km. Because of this slope, we would expect more mode coupling to occur than in the FLAT environments. Thus, accurate modeling of this propagation is expected to be more challenging.

The solutions for the 250 Hz and 500 Hz sources are displayed in Figs. 19 and 20, respectively. As before, the results agree well at short range and begin to degrade at longer ranges. In this case, however, we find that some phase errors begin to appear for even the large-scale features at ranges beyond about 15 km.

IWc

This environment contains the most complicated water column sound speed structures of all the test cases. The bottom is a simple, homogeneous half-space with a smooth interface at 200

m. The background water column profile is also relatively simple, defined using a typical shallow water, downward-refracting canonical profile with a minimum at the bottom depth of 200 m, and surface duct from 0 to 26 m. However, this background profile in the water column is perturbed by a train of five solitons superimposed upon five sinusoidal linear internal waves of scales 500 m to 1700 m.

The solutions for the 250 Hz and 500 Hz sources are displayed in Figs. 21 and 22, respectively. Once again, we find the results agree well at short range and begin to degrade at longer ranges. This suggests that the MMPE model is quite capable of dealing with complicated sound speed structures in the water column. The real challenge for this model appears to be in the treatment of the bottom interface condition.

Broadband Pulse Propagation: FLATa

Finally, we examine some results from the FLATa environment when the broadband source is modeled. The source is again placed at a depth of 30 m but now has a finite bandwidth. The definition of the source spectrum was based on a Gaussian function centered at 375 Hz and a Gaussian half-width of 80 Hz. As stated in Section II, the MMPE model produces single frequency solutions which can then be Fourier synthesized to generate pulse propagation predictions. In general, any source spectrum could be used to scale the individual frequency components. The post-processing software of the MMPE model assumes a simple, Hanning window form for the source spectrum. Since the specific details of the spectrum were not the issue but rather the bandwidth and temporal resolution, the default Hanning window was used with a total bandwidth of 175 Hz. This is comparable to the defined Gaussian spectrum.

In order to avoid wrap-around of the signal in the time domain, a total time window of roughly 1.5 seconds was needed. Thus, a minimum of 256 single-frequency calculations was required, evenly spaced over the bandwidth. To insure that there was no influence from wrap-around, the following data was run with 512 single-frequency calculations. Due to the higher frequencies involved, a range step of 2.5 m was chosen while the depth mesh was set to ~ 0.4 m. Note that the wavelength varies from roughly 5 m down to 3 m over this bandwidth, and so our convergence and stability conditions on the mesh sizes are roughly satisfied for all frequencies.

For these settings, each CW run takes about 45 sec to complete. The total time for this pulse prediction is then roughly 6 hours. Because this scales linearly with the number of single frequency runs completed, we are motivated to consider using smaller bandwidths. This will reduce our temporal resolution of the multipath structure, but may be worthwhile if we can significantly reduce the run-time. Therefore, a second calculation was done with only 128 frequencies over a total (Hanning window) bandwidth of 80 Hz. This reduces the calculation to just over 1 1/2 hours, a much more manageable time. The results for each of these calculations are given in Fig. 23 for a receiver at range 20 km and depth 35 m.

Significant differences are noted between the two solutions which are beyond simple temporal resolution issues. Two possible causes may be suggested. First, we assume both solutions are accurate for their given bandwidths, and the differences arise because of effects at the upper and lower ranges of the larger bandwidth which generate more interference and appear to reduce the average levels near 13.6, 13.8, and 14 secs. Second, that the upper and lower ranges

of the larger bandwidth are not as accurate as necessary due to being further away from the optimal values of the range and depth mesh sizes. (Note that the smaller bandwidth results end before the larger bandwidth simply due to a reduction in the total time window for the latter calculation. This would not be expected to introduce the observed differences.)

Unfortunately, neither of the models of Mikhin or Brooke, et al., were used to generate predictions of the broadband pulse propagation. So any comments on the accuracy of these results are purely speculative. However, it should be noted that the broadband results can show some of the same sensitivity to the computational mesh sizes as the CW runs. An example of this is given in Fig. 24 which compares the previous, wide bandwidth results with those computed using an increased mesh size of $\Delta r = 5$ m and $\Delta z \approx 1.6$ m.

Clearly these results do not compare favorably for the later arrivals corresponding to the higher modes. This may be consistent with the previous issues encountered with the mixing lengths, which could be expected to effect the higher modes more significantly than the lower modes. Still, without a benchmark solution for comparison, no formal analysis of this effect has been performed

FLATa: Random Perturbations

Finally, we consider a very important point regarding the accuracy of the MMPE model predictions. Although the environments defined are considered to have "realistic" fluctuations, they are still idealized in the sense that the environment is defined *exactly.* But what impact do unknown perturbations have on the solutions, even those considered of benchmark quality?

To examine this issue, we return to the FLATa environment with the 250 Hz source transmission. In addition to the specified environment, we now add a random 1% error to the depth (still range-independent), the bottom sound speed and sound speed gradient, the density, and the attenuation. A 0.1% random error is added to the water column sound speed (still homogeneous). This was accomplished simply by generating a random number between -1 and 1 for each of the parameters affected, and then multiplying by the appropriate percentage (i.e., either 0.01 or 0.001). The parameter value was then altered by adding this percentage variation.

The results of two such randomized perturbations are compared to the unperturbed MMPE solution in Fig. 25. While the discrepancies between these results are not as severe as those compared with Mikhin's solution, they still show a relatively high degree of variability in the fine-scale structure at ranges beyond about 10 km. Thus, one could certainly argue that, in real ocean environments, point-wise predictions of acoustic propagation are not possible at 100's of water depths in shallow water. General trends are probably possible, and PE/SSF models, if properly used, can produce quite accurate results to this resolution. Such models also have the advantage of being highly efficient, numerically stable, and may even be automated to produce acceptable predictions of acoustic propagation.

Other SWAM'99 Test Cases

Solutions for the other SWAM'99 test cases using the criteria determined from this analysis are, at the time of this writing, still being catalogued. They will be available on the

SWAM'99 ftp site for other investigators to examine. They can also be provided directly to anyone by contacting the author via e-mail.

V. Conclusions

In this paper, a detailed description of the Monterey-Miami Parabolic Equation (MMPE) model was given along with an exhaustive analysis of its predictions in several shallow water environments defined in the SWAM'99 Workshop. Much of the model development is similar to other parabolic equation models based on other numerical algorithms. The MMPE model employs the split-step Fourier numerical algorithm to march the solution to the acoustic field out in range. It was shown that, while this algorithm is one of the most highly efficient numerical approaches, it introduces other complexities which make point-wise predictions in explicitly defined environments difficult. Much of this is related to the treatment of the bottom interface boundary condition, which must be treated numerically in terms of smooth, generalized mixing functions used to simulate the discontinuous nature of the boundary. Such problems do not occur in the models developed by other researchers,[24],[25] which explicitly treat the parabolic approximation on the boundaries of finite elements by higher order numerical methods. Not only are these methods higher order in their approximation of the square root operator, but they directly treat the proper boundary condition across the boundary interfaces. However, such methods are generally more computationally intensive. They must also consider the proper treatment of vertical boundary conditions in range-dependent environments in order to maintain proper energy conservation. Such energy conservation is intrinsic in the development of the SSF/PE algorithm used in the MMPE model.

The sound speed discontinuity, relatively simple to define, is treated with a smooth hyperbolic mixing function. In order to properly sample this function, the mixing length must be at least one depth mesh. Furthermore, the scale of the mixing length used to produce the most accurate results was found to be $L_c \sim \lambda/10$. The small scale relative to a wavelength is not too surprising since we are attempting to model a step function discontinuity. However, smaller mixing lengths were found to degrade the solution. The exact cause is unclear, but is presumably due to either numerical problems associated with the environmental propagator function or numerical noise resulting from the Fourier synthesis of a sharp discontinuity. In addition, larger mixing lengths did not perform well, presumably due simply to the poor simulation of a discontinuous interface.

The density discontinuity is a much more difficult issue to treat, particularly with mixing functions. Part of the difficulty is in the form of the effective index of refraction which contains both the second derivative of the density with respect to depth, but also the square of the first derivative. It was argued that only the former can properly be modeled with generalized functions, and should produce accurate results with small mixing lengths. However, this function is simulating the first derivative of a delta function, which is difficult to do over a small depth. A well defined cubic spline function was employed to model this interface. For this function, at least two depth meshes are required to properly sample the function. Analysis showed that the optimal mixing length was $L_\rho \sim 2\lambda$.

Finally, an analysis of the solution accuracy with range step size was performed. The best solution was found when $\Delta r \sim \lambda$. Furthermore, unlike other numerical algorithms, it was shown that solutions based on the split-step Fourier algorithm actually degrade as the range step is decreased further. This is due to the form of the propagator functions which no longer provide enough phase information per range step for values much less than a wavelength.

This analysis of optimal mixing lengths and mesh sizes proved to be a challenging exercise. Convergence of the solutions was not obtained by continually decreasing the mesh sizes, but rather stability was used to define the best solutions. This also limits the accuracy of spatial points which do not fall on a grid point to the interpolation scheme employed. Still, it was comforting to find that the model did satisfy the requirement of reciprocity out to the longest ranges specified to within 1% in amplitude and two-tenths of a degree in phase.

With these findings, predictions of the acoustic propagation for several of the SWAM'99 test cases were made. These results were compared to those generated by another parabolic equation model which was thought to produce high quality solutions. It was found that these predictions compared quite well at short range (less than ~ 10 water depths), including the small scale fluctuations. This appeared independent of frequency, suggesting that there are specific ray-like paths which exhibit the sensitivity to the treatment of the bottom interface condition. At longer ranges, the larger scale features of the solutions also compared well. This was consistently found to be true for all environments at all frequencies considered, with the slight exception of the lowest frequency problems which contained only a few propagating modes within the waveguide.

The results did suggest potential problems with the model for very low-frequency sources due to the finite extent of the density mixing function. In this sense, low frequency is defined in terms of the number of wavelengths or modes which can fit within the water column. In the FLATa case considered here, the water depth was only about one and a half times the wavelength. Thus, the mixing function extended throughout most of the water column, significantly perturbing the environment we were attempting to model.

The accuracy that should be required of any propagation model should be put in the context of our ability to accurately define the environment. To address this issue, minor random perturbations were added to one test case. It was found that the variability introduced in the solutions due to these perturbations was of the same order as the differences between the MMPE solutions and Mikhin's solutions. Thus, one may conclude that the MMPE produces solutions which are just as accurate as a benchmark quality model given a real ocean environment with inherent uncertainties. The efficiency of this PE/SSF model in producing both CW and broadband pulse predictions makes it an attractive and powerful tool for ocean acoustic propagation modeling.

Results from a broadband calculation were also presented. However, due to a lack of other model results for comparison, the accuracy of such results is unknown. It is hoped that developers of the benchmark quality models will attempt to produce broadband results for comparison in the future.

Finally, potential improvements to the model should be mentioned. Because much of the difficulty in finding stable, convergent solutions resulted from the treatment of the bottom, other approaches should be considered. One attractive alternative may be related to the recently developed non-local boundary treatments which are able to produce the required reflection condition without having to directly account for the field penetrating below the interface.[26] Unfortunately, this approach is not currently suitable for implementation within the split-step Fourier algorithm.

Additionally, it is known that the WAPE approximation used in the model does introduce phase errors which accumulate with range. In fact, these errors could certainly be a contributing factor to the fine-scale mismatch observed at longer ranges. Tappert's c_0-insensitive method has been shown to significantly reduce these phase errors in this approximation.[27] The addition of this approach to the MMPE model is currently being attempted, and any improvement in the model's accuracy will be reported in the near future.

Acknowledgments

The author would like to sincerely thank Prof. Frederick Tappert of the University of Miami for his many contributions in the development of this model. Much of this work was based on concepts and ideas based on his own research and efforts. This work was supported by the Office of Naval Research, Code 321OA.

References

1 Jensen, F. B., Kuperman, W. A., Porter, M. B., and Schmidt, H., *Computational Ocean Acoustics* (AIP, New York, 1994), pp. 131-133 (1994).

2 Nghiem-Phu, L. and Tappert, F. D., "Modeling of reciprocity in the time domain using the parabolic equation method," J. Acoust. Soc. Am. **78**, pp. 164-171 (1985).

3 Smith, K.B. and Tappert, F.D., "UMPE: The University of Miami Parabolic Equation Model, Version 1.0," Marine Physical Laboratory Technical Memo 432 (1993).

4 Tappert, F. D., "The parabolic approximation method," in Lecture Notes in Physics, Vol. 70, *Wave Propagation and Underwater Acoustics*, edited by J. B. Keller and J. S. Papadakis (Springer-Verlag, New York), pp. 224-287 (1977).

5 Hardin, R. H. and Tappert, F. D., "Applications of the split-step Fourier method to the numerical solution of nonlinear and variable coefficient wave equations," SIAM Rev. **15**, p. 423 (1973).

6 Lee, D., Botseas, G., and Papadakis, J. S., "Finite-difference solution to the parabolic wave equation," J. Acoust. Soc. Am. **70**, pp. 795-800 (1981).

7 Collins, M. D., “Benchmark calculations for higher-order parabolic equations,” J. Acoust. Soc. Am. **87**, pp. 1535-1538 (1990).

8 Collins, M. D. and Westwood, E. K., “A higher-order energy-conserving parabolic equation for range-dependent ocean depth, sound speed, and density,” J. Acoust. Soc. Am. **89**, pp. 1068-1075 (1991).

9 Collins, M. D., Cederberg, R. J., King, D. B., and Chin-Bing, S. A., “Comparison of algorithms for solving parabolic wave equations,” J. Acoust. Soc. Am. **100**, pp. 178-182 (1996).

10 Sakurai, J. J., *Modern Quantum Mechanics* (Benjamin/Cummings, Menlo Park, CA), pp. 72-73 (1985).

11 Thomson, D. J. and Chapman, N. R., “A wide-angle split-step algorithm for the parabolic equation,” J. Acoust. Soc. Am. **74**, pp. 1848-1854 (1983).

12 Fawcett, J. A., “Modeling three-dimensional propagation in an oceanic wedge using parabolic equation methods,” J. Acoust. Soc. Am. **93**, pp. 2627-2632 (1993).

13 Smith, K.B., “A three-dimensional propagation algorithm using finite azimuthal aperture,” J. Acoust. Soc. Am. **106**, pp. 3231-3239 (1999).

14 Bellman, R., *Perturbation Techniques in Mathematics, Physics, and Engineering* (Holt, Rinehart, and Winston, Inc., New York), pp. 38-39 (1964).

15 Jensen, F. B., Kuperman, W. A., Porter, M. B., and Schmidt, H., *Computational Ocean Acoustics* (AIP, New York, 1994), pp. 379-381 (1994).

16 Tappert, F. D., Spiesberger, J. L. and Boden, L., “New full-wave approximation for ocean acoustic travel time predictions,” J. Acoust. Soc. Am. **97**, pp. 2771-2782 (1995).

17 Lighthill, M. J., *Introduction to Fourier analysis and generalised functions* (Cambridge University Press, New York), p. 79 (1958).

18 Tappert, F. D., “The c_0-Independent PE Model: Analysis of Sound Speed Discontinuity,” unpublished lecture notes (1991).

19 Chin-Bing, S. A., King, D. B., Davis, J. A., and Evans, R. B., eds., “PE Workshop II: Proceedings of the 2nd Parabolic Equation Workshop, May 6-9, 1991,” Naval Research Laboratory - Stennis Space Center, NRL Book Contribution (1993).

20 Yevick, D. and Thomson, D. J., “A hybrid split-step/finite-difference PE algorithm for variable-density media,” J. Acoust. Soc. Am. **101**, pp. 1328-1335 (1997).

21 Thomson, D. J. and Bohun, C. S., “A wide-angle initial field for the parabolic equation models,” J. Acoust. Soc. Am. **83**, p. S118 (1988).

22 Tindle, C. T. and Zhang, Z. Y., “An equivalent fluid approximation for a low shear speed ocean bottom,” J. Acoust. Soc. Am. **91**, pp.3248-3256 (1992).

23 Zhang, Z. Y. and Tindle, C. T., “Improved equivalent fluid approximations for a low shear speed ocean bottom,” J. Acoust. Soc. Am. **98**, pp. 3391-3396 (1995).

24 Brooke, G., Thomson, D. J., and Ebbeson, G., “Canadian Parabolic Equation (PECan) Results for Some 2D and 3D Shallow Water Test Cases,” ***** SWAM’99 Workshop*****.

25 Mikhin, D., “Energy-conserving and reciprocal solutions for higher-order parabolic equations,” ***** SWAM’99 Workshop*****.

26 Yevick, D. and Thomson, D.J., “Nonlocal boundary conditions for finite-difference parabolic equation solvers,” J. Acoust. Soc. Am. **106**, pp. 143-150 (1999).

27 Tappert, F. D., “New c0-insensitive version of the PE/SSF model,” ***** SWAM’99 Workshop*****.

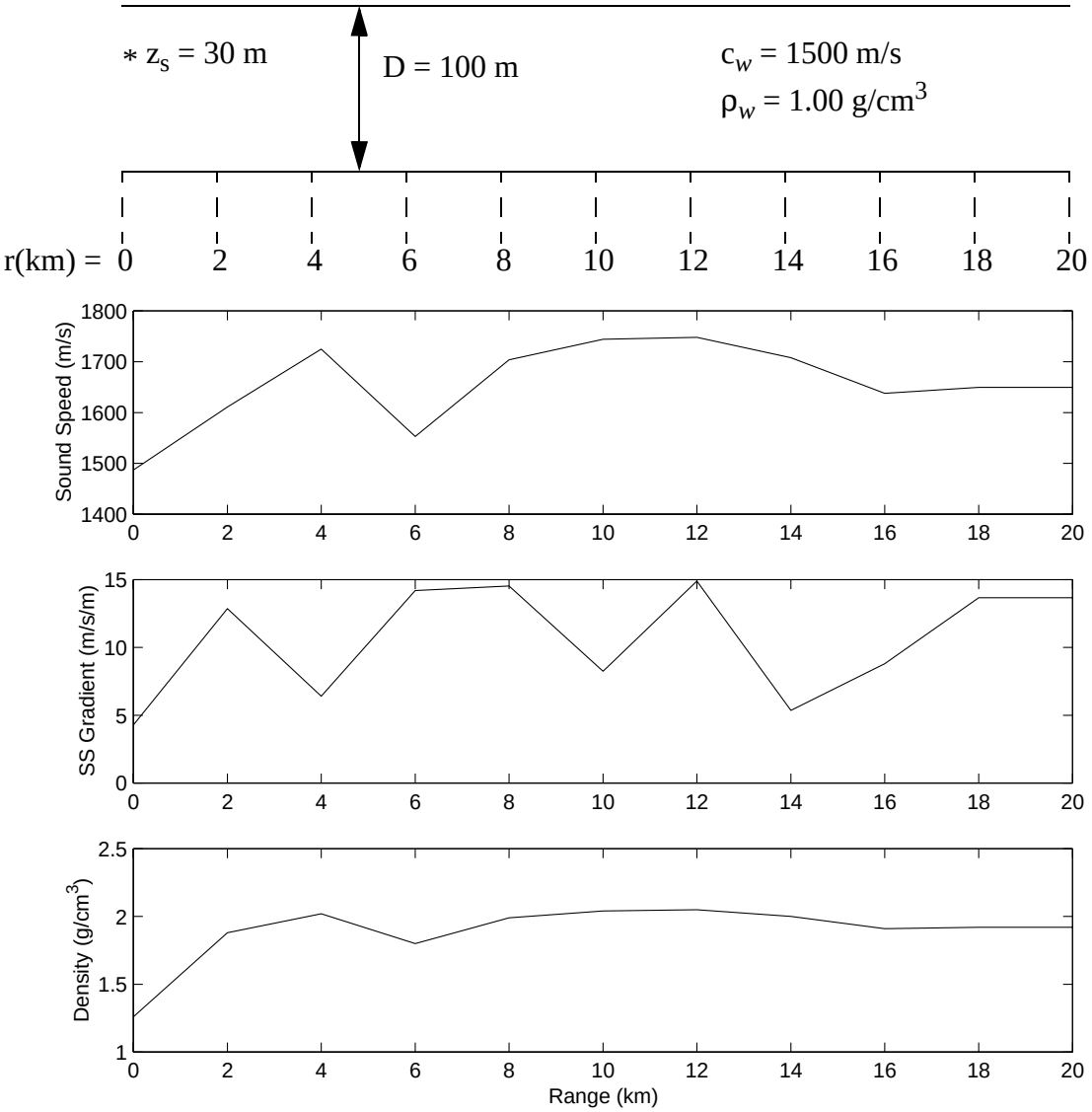

Figure 1: The FLATa test case environment. The water column is homogeneous and the range-dependent bottom acoustic parameters are shown linearly interpolated as the model treats the input.

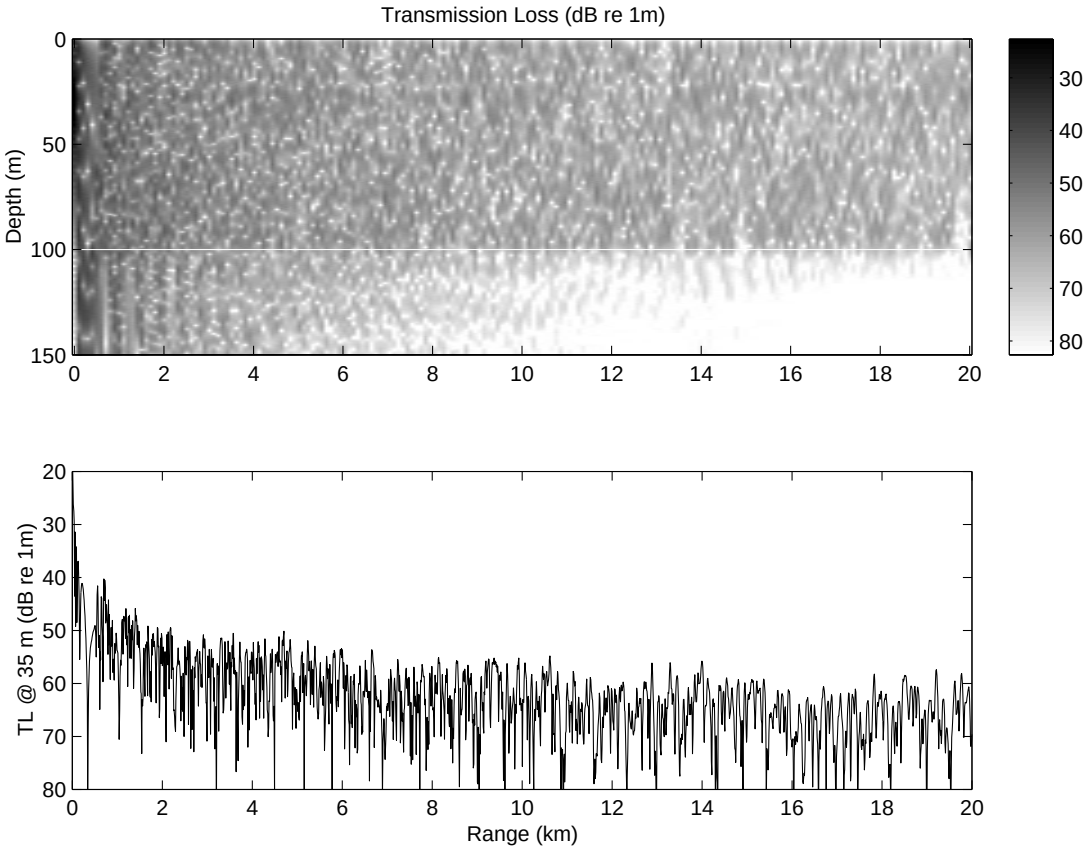

Figure 2: MMPE model solution for the FLATa environment with a 250 Hz CW source at 30 m. Upper panel shows the complete two-dimensional field in the water column while the lower panel displays the transmission loss trace at a receiver depth of 35 m.

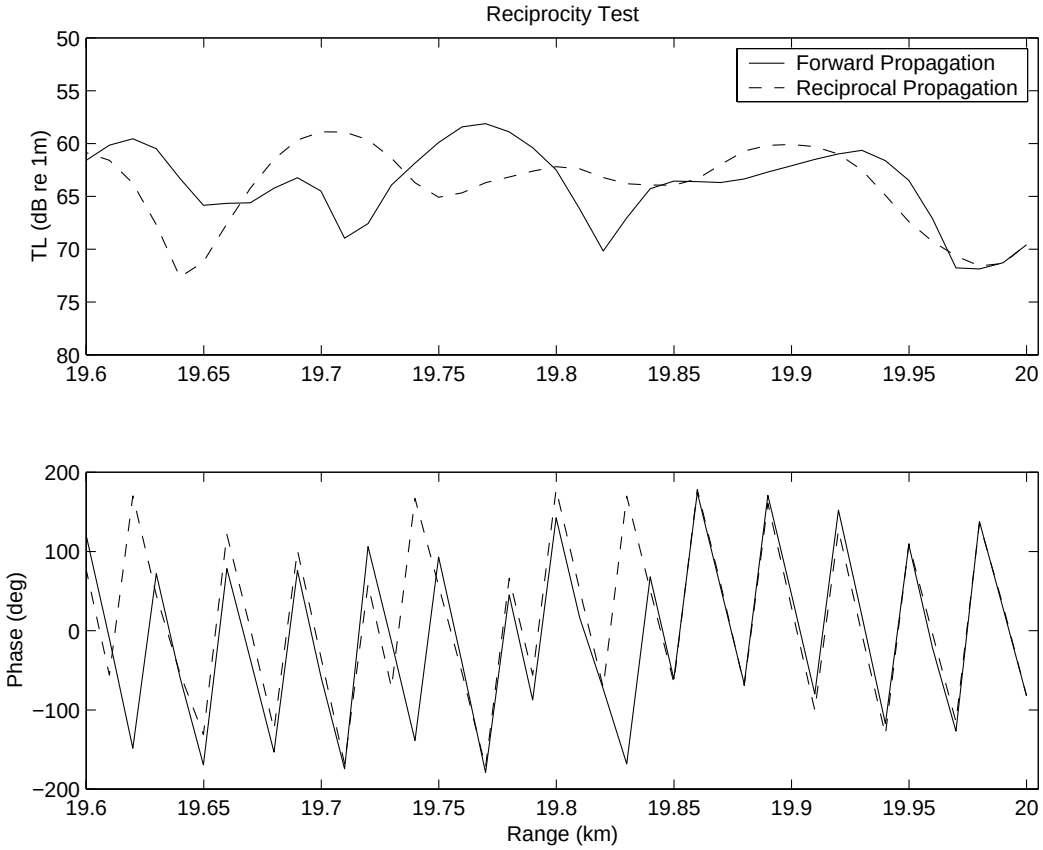

Figure 3: Results of reciprocity test for the FLATa environment. Upper panel shows TL trace at reciprocal depths while the lower plot displays the acoustic phase at each depth. The “Forward Propagation” results correspond to a 250 Hz CW source at 30 m and receiver at 35 m while the inverse is true for the “Reciprocal Propagation”.

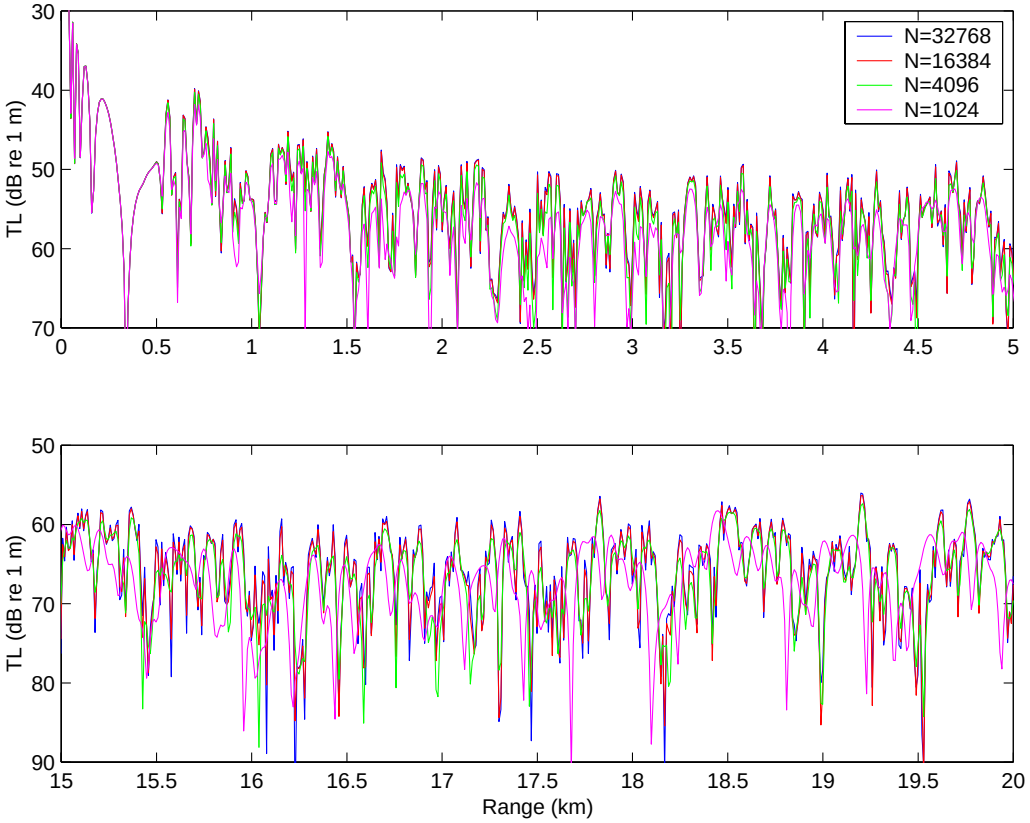

Figure 4: Convergence testing for various transform sizes used in the PE/SSF algorithm. The maximum depth of the "real" ocean is 400 m, so the depth mesh size is determined from $\Delta z = 800/N$ (including the image ocean). Upper and lower panels show the first and last 5 km of the solution, respectively.

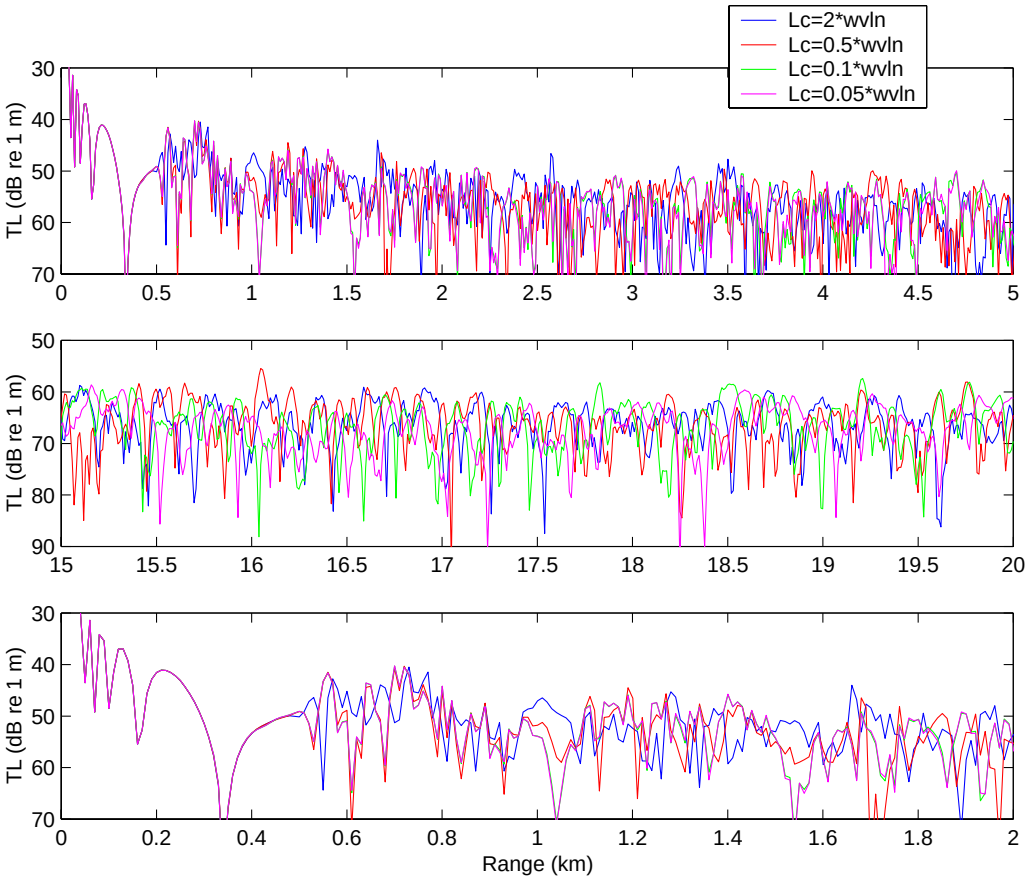

Figure 5: Convergence testing for various values of the bottom interface sound speed mixing length relative to an acoustic wavelength. Upper and middle panels show the first and last 5 km of the solution, respectively, while the lower plot displays an enhanced view of the first 2 km.

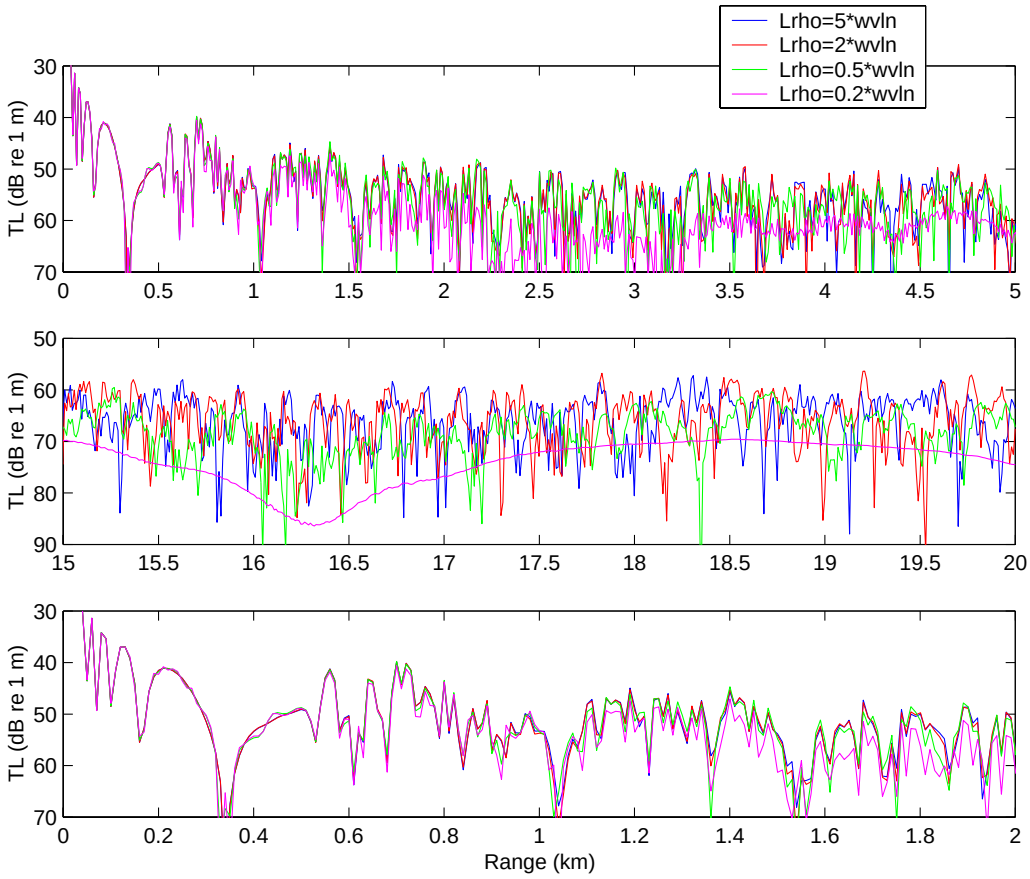

Figure 6: Convergence testing for various values of the bottom interface density mixing length relative to an acoustic wavelength. Upper and middle panels show the first and last 5 km of the solution, respectively, while the lower plot displays an enhanced view of the first 2 km.

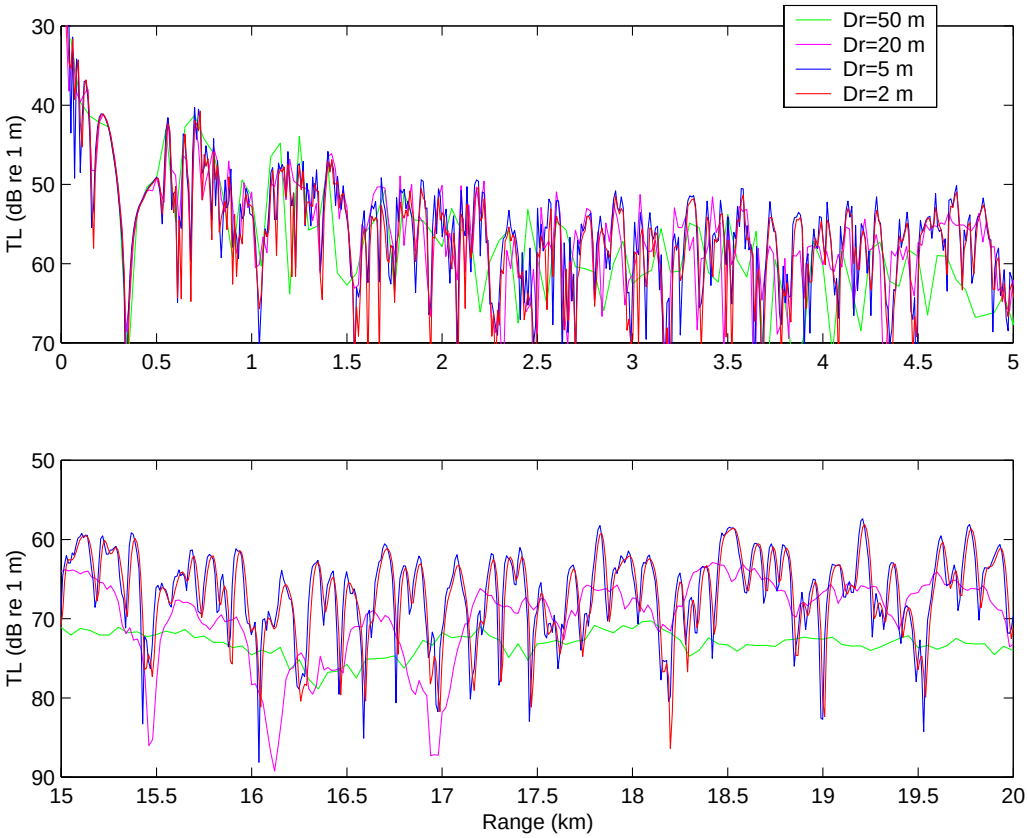

Figure 7: Convergence testing for various range step sizes, Δr. Upper and lower panels show the first and last 5 km of the solution, respectively.

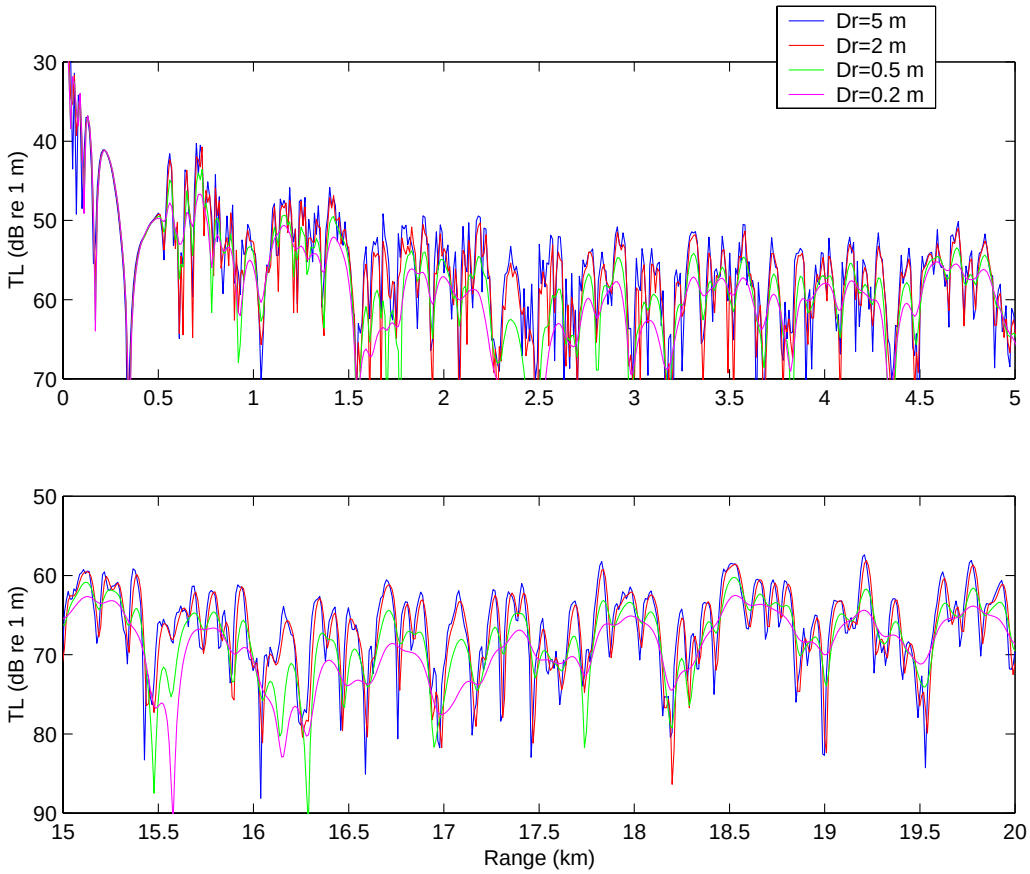

Figure 8: Stability analysis for range step sizes smaller than the optimal. Upper and lower panels show the first and last 5 km of the solution, respectively.

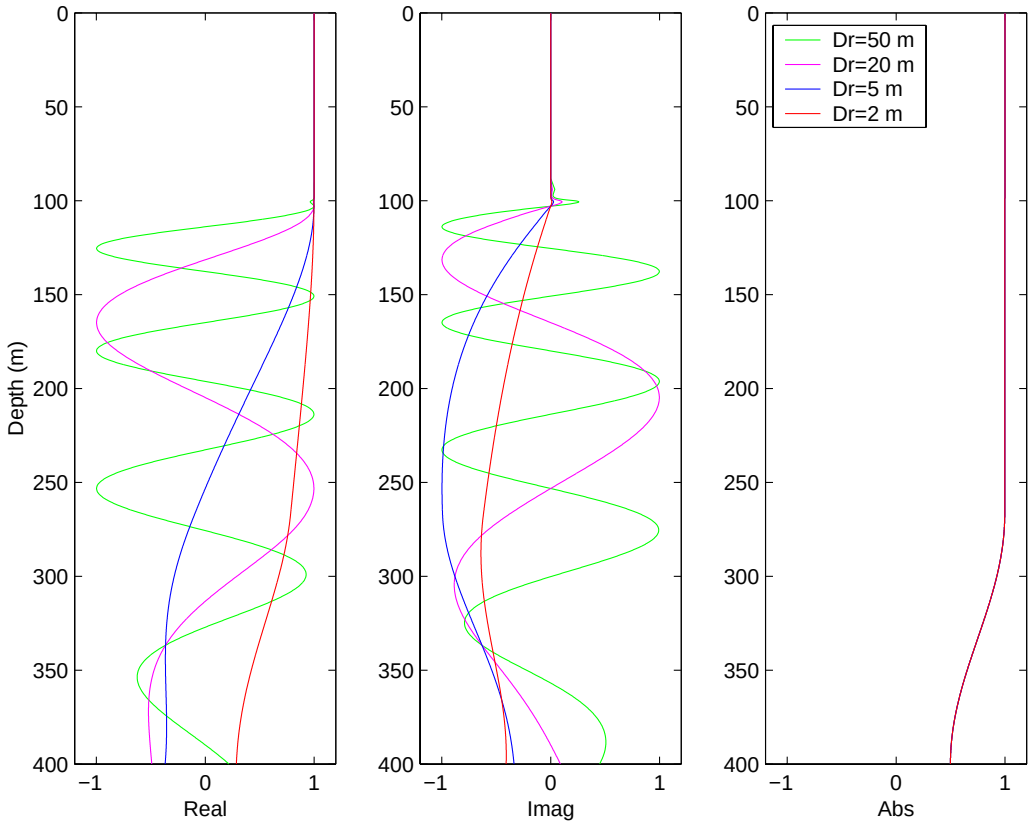

Figure 9: *z*-space propagator function for the various values of range step used to generate the data in Fig. 7.

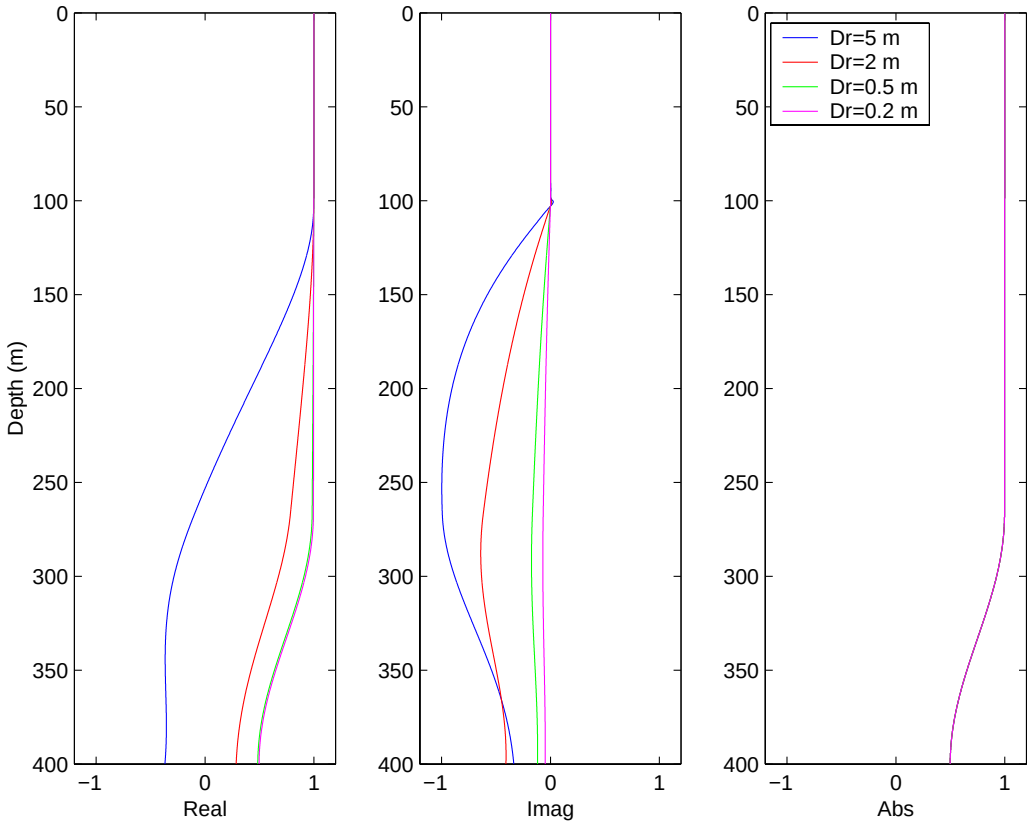

Figure 10: *z*-space propagator function for the various values of range step used to generate the data in Fig. 8.

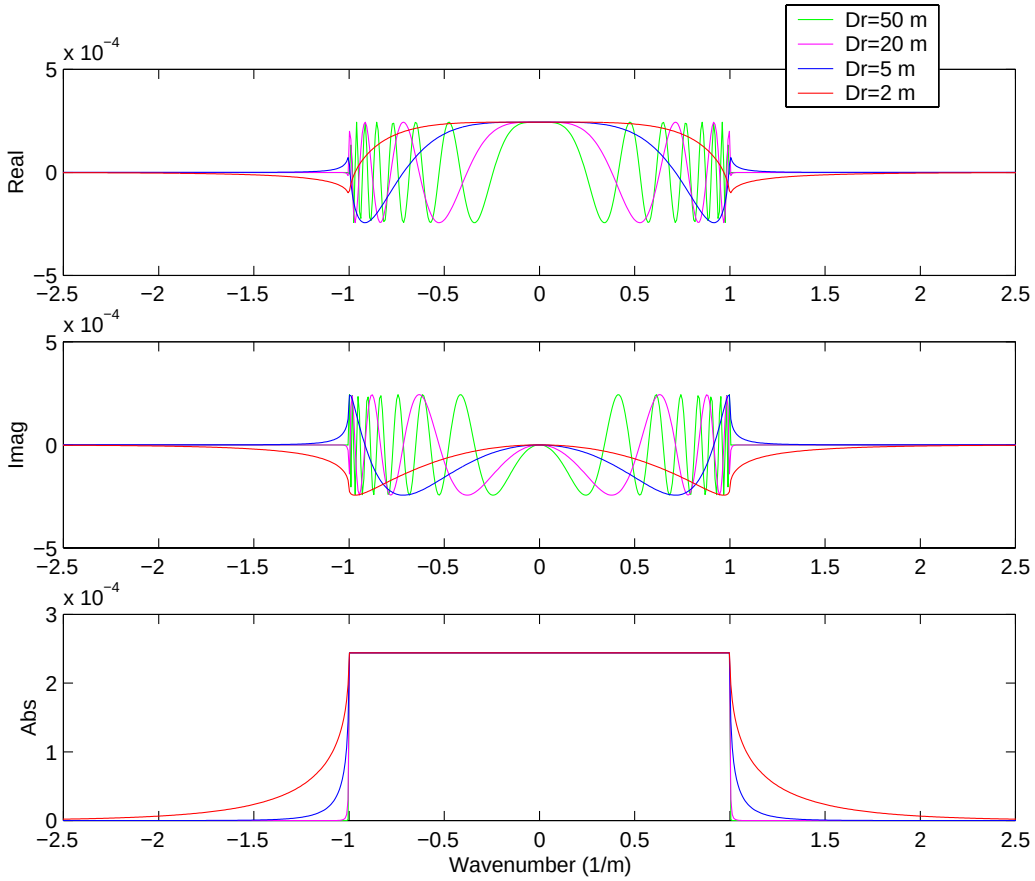

Figure 11: k_z-space propagator function for the various values of range step used to generate the data in Fig. 7.

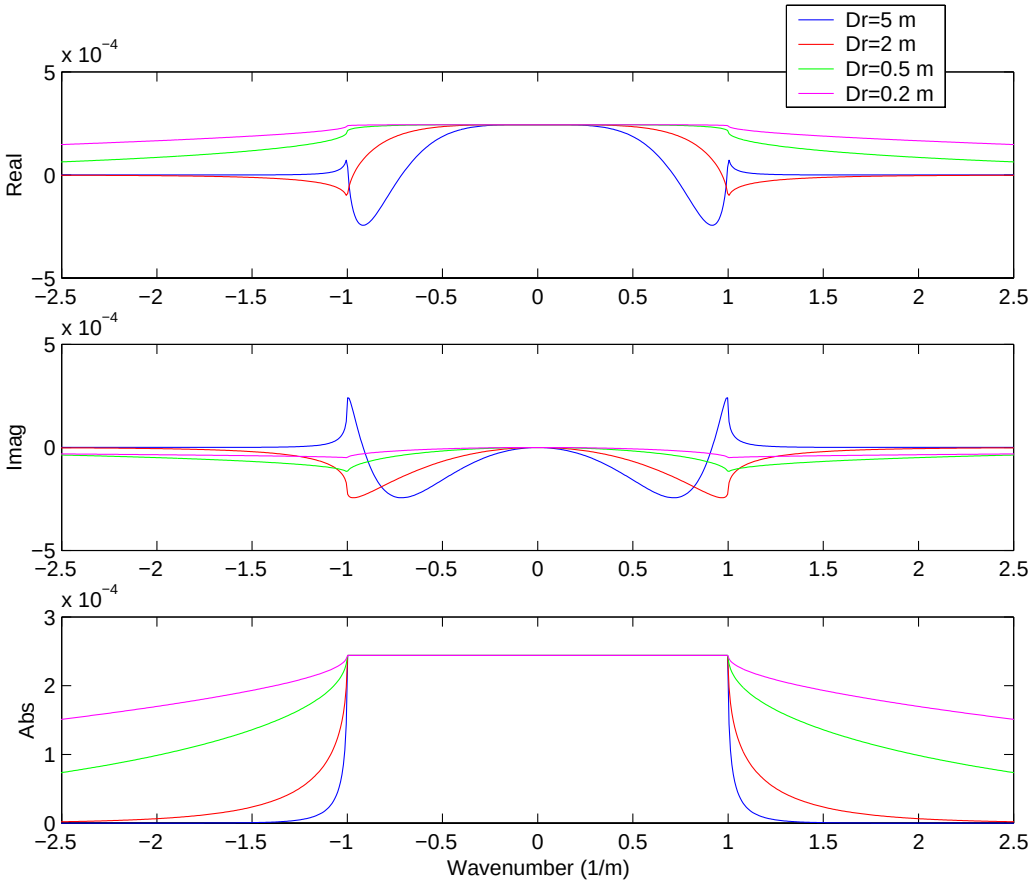

Figure 12: k_z-space propagator function for the various values of range step used to generate the data in Fig. 8.

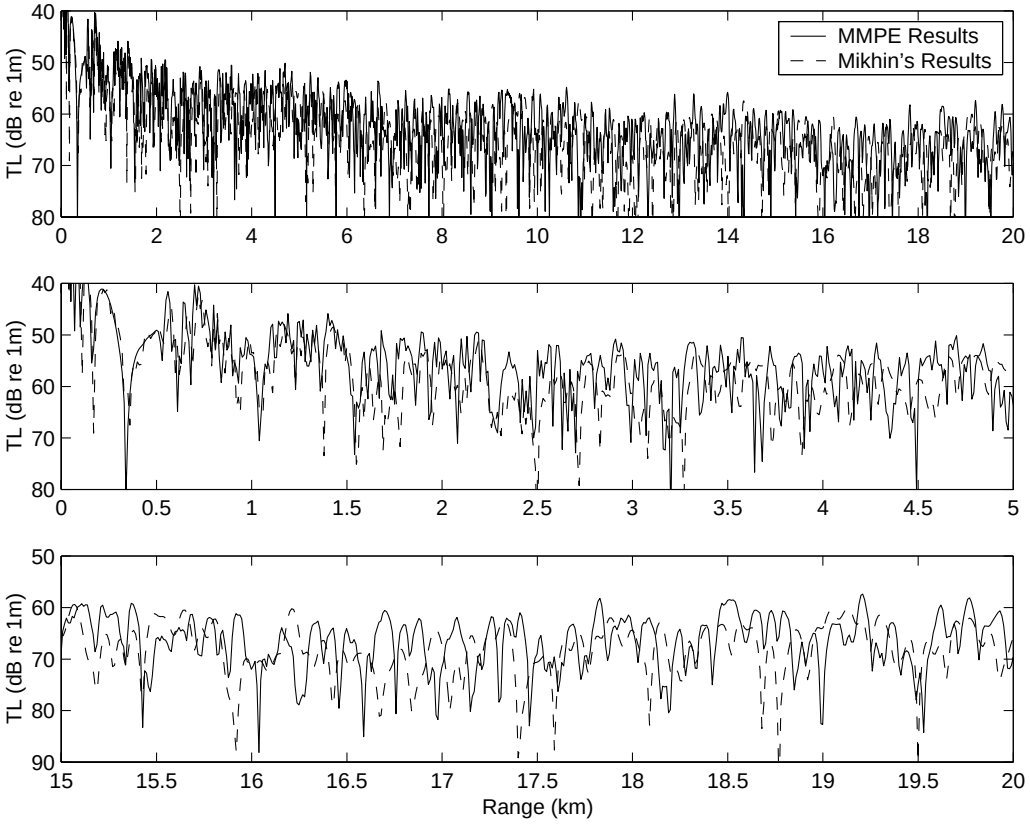

Figure 13: Comparison of MMPE results with Mikhin's results for the FLATa environment generated by Dmitry Mikhin. The source corresponds to the 250 Hz CW source at 30 m depth. Upper panel displays the complete TL trace at 35 m, while the middle and lower panels provide an enhanced view of the first and last 5 km, respectively. For this run, $\Delta z = 0.03\lambda$ and $\Delta r = \lambda$.

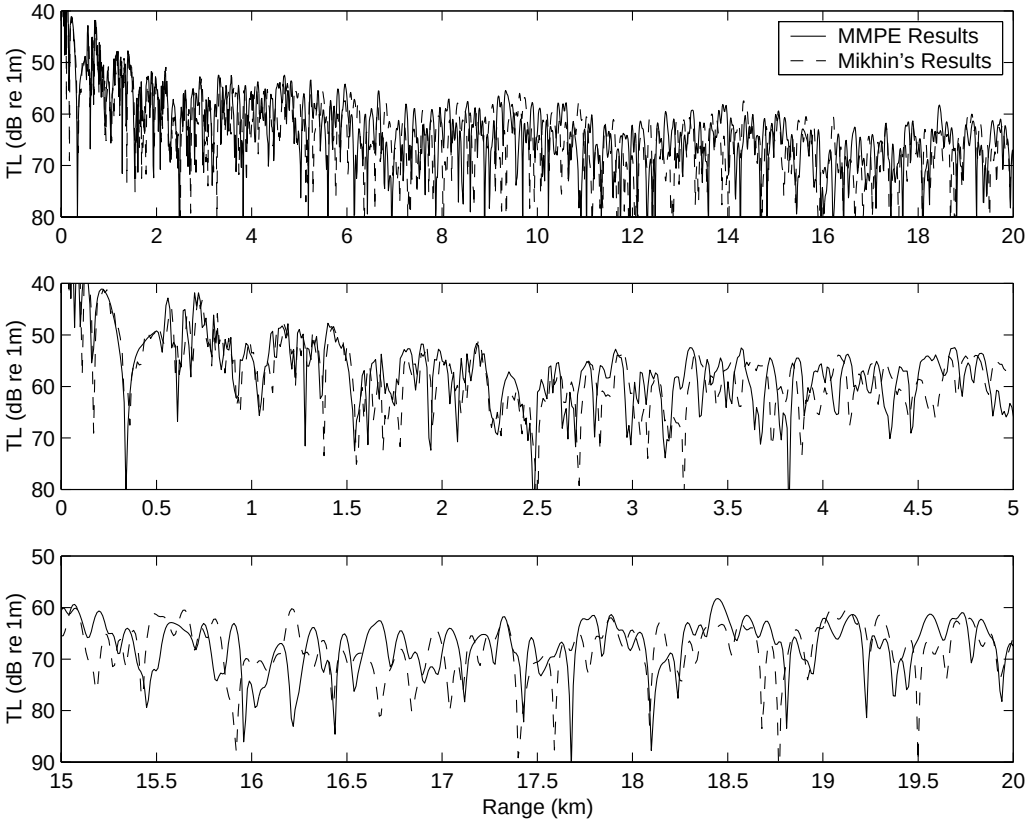

Figure 14: Comparison of MMPE results with Mikhin's results for depth mesh value $\Delta z = 0.13\lambda$ and range step $\Delta r = \lambda$. The source corresponds to the 250 Hz CW source at 30 m depth.

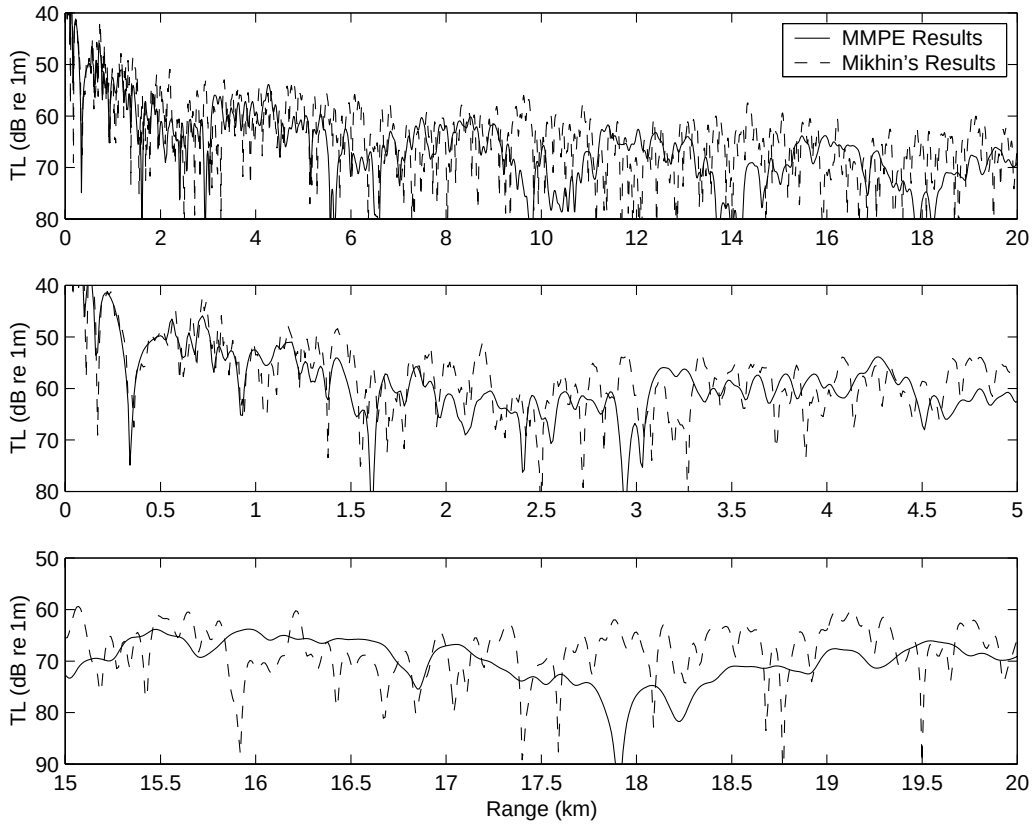

Figure 15: Comparison of MMPE results with Mikhin's results for depth mesh value $\Delta z = 0.5\lambda$ and range step $\Delta r = \lambda$. The source corresponds to the 250 Hz CW source at 30 m depth.

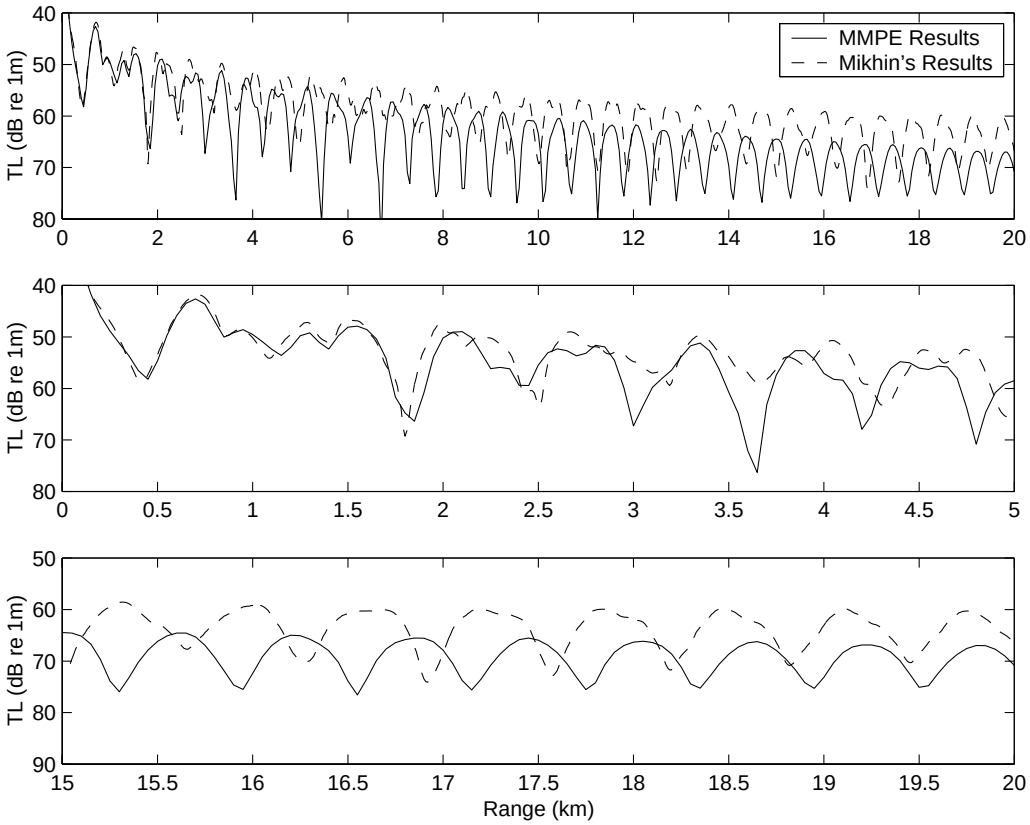

Figure 16: Comparison of optimal MMPE results with Mikhin's results for the FLATa environment. The source corresponds to the 25 Hz CW source at 30 m depth.

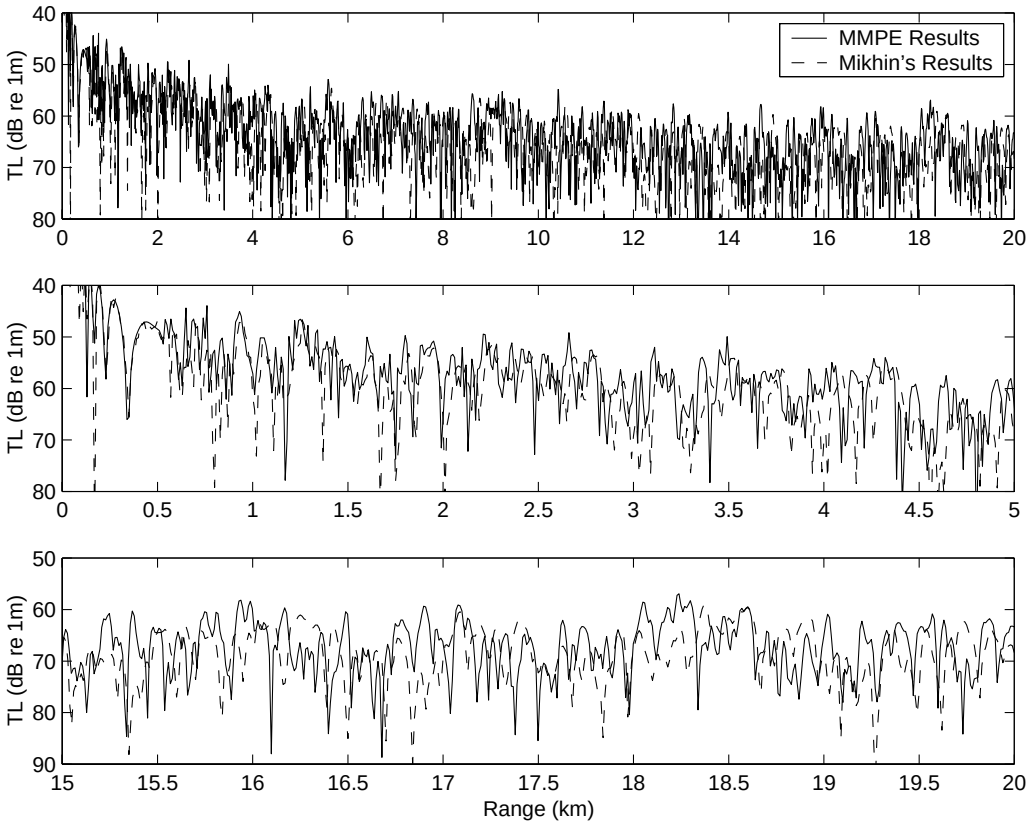

Figure 17: Comparison of optimal MMPE results with Mikhin's results for the FLATa environment. The source corresponds to the 500 Hz CW source at 30 m depth.

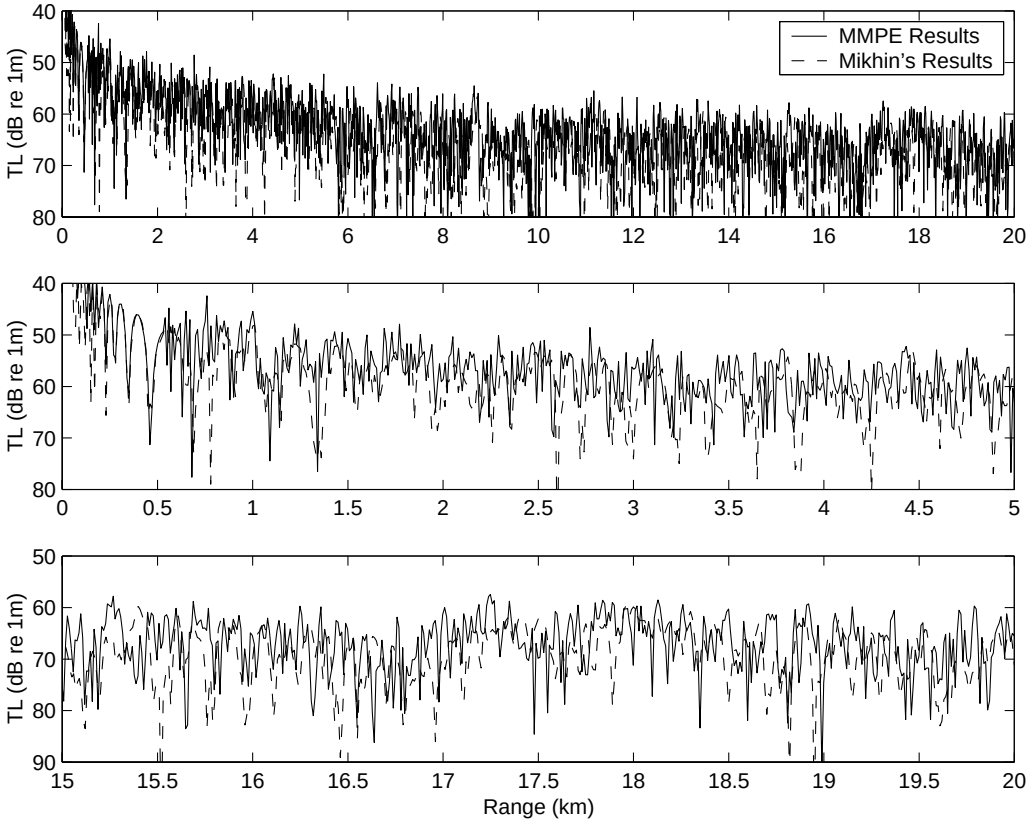

Figure 18: Comparison of optimal MMPE results with Mikhin's results for the FLATa environment. The source corresponds to the 1000 Hz CW source at 30 m depth.

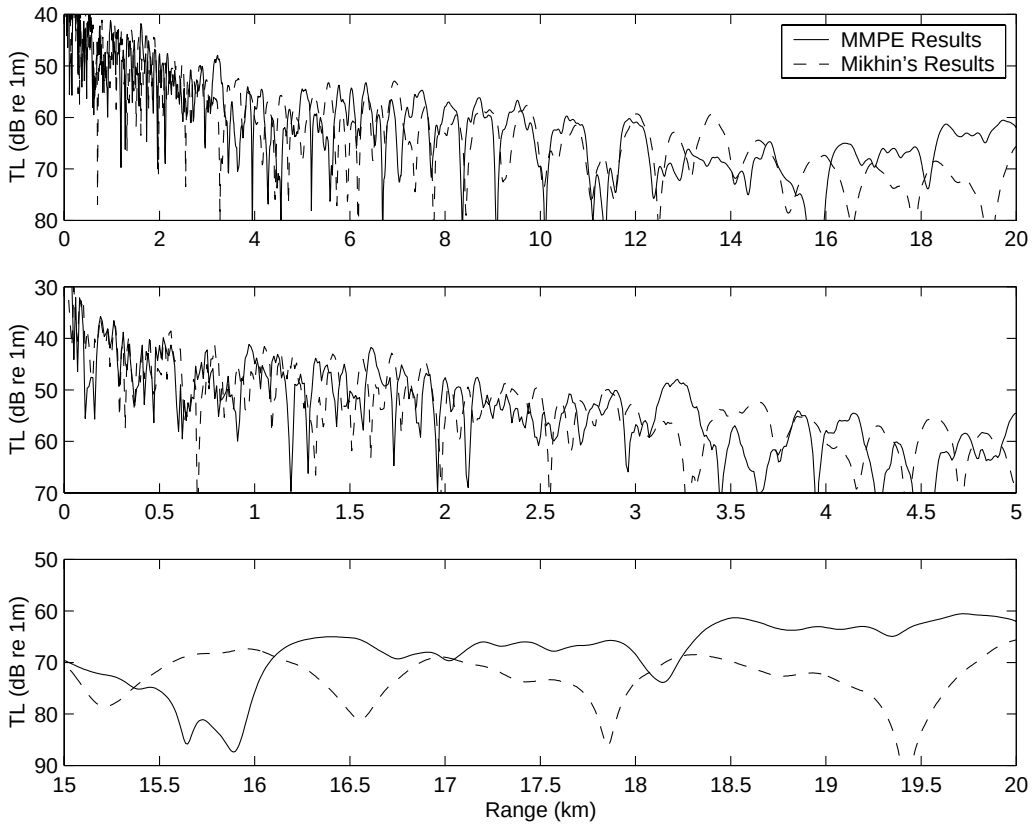

Figure 19: Comparison of optimal MMPE results with Mikhin's results for the DOWNa environment. The source corresponds to the 250 Hz source at 30 m depth.

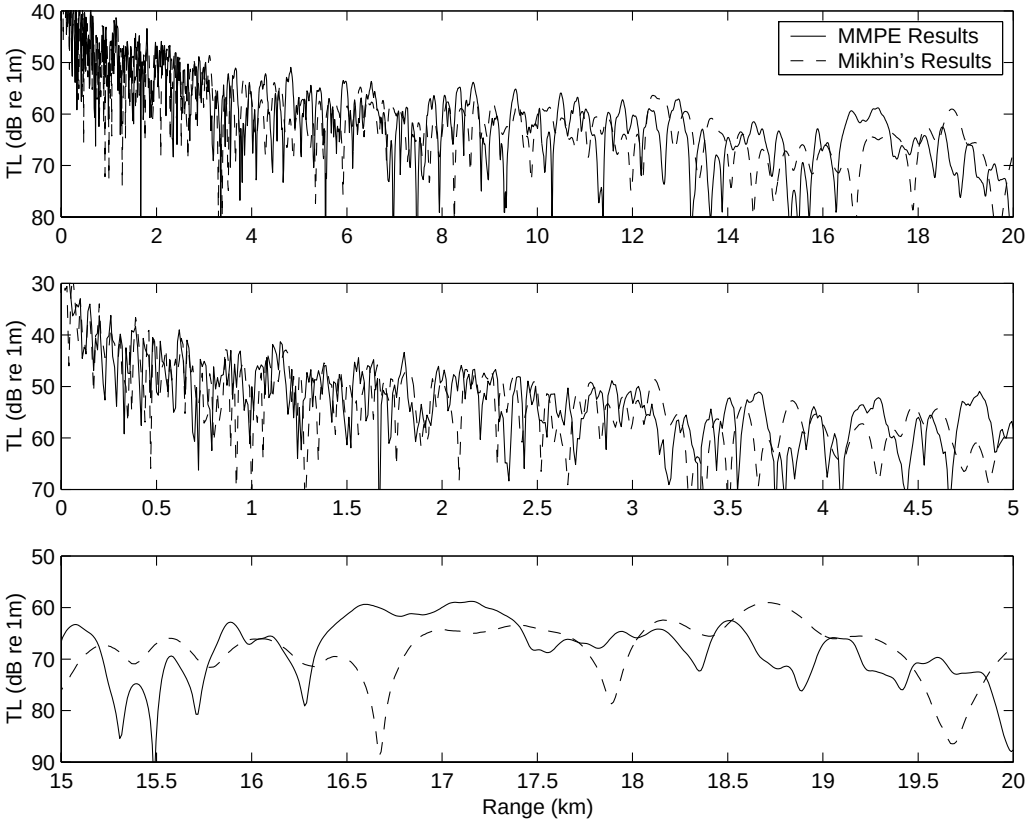

Figure 20: Comparison of optimal MMPE results with Mikhin's results for the DOWNa environment. The source corresponds to the 500 Hz CW source at 30 m depth.

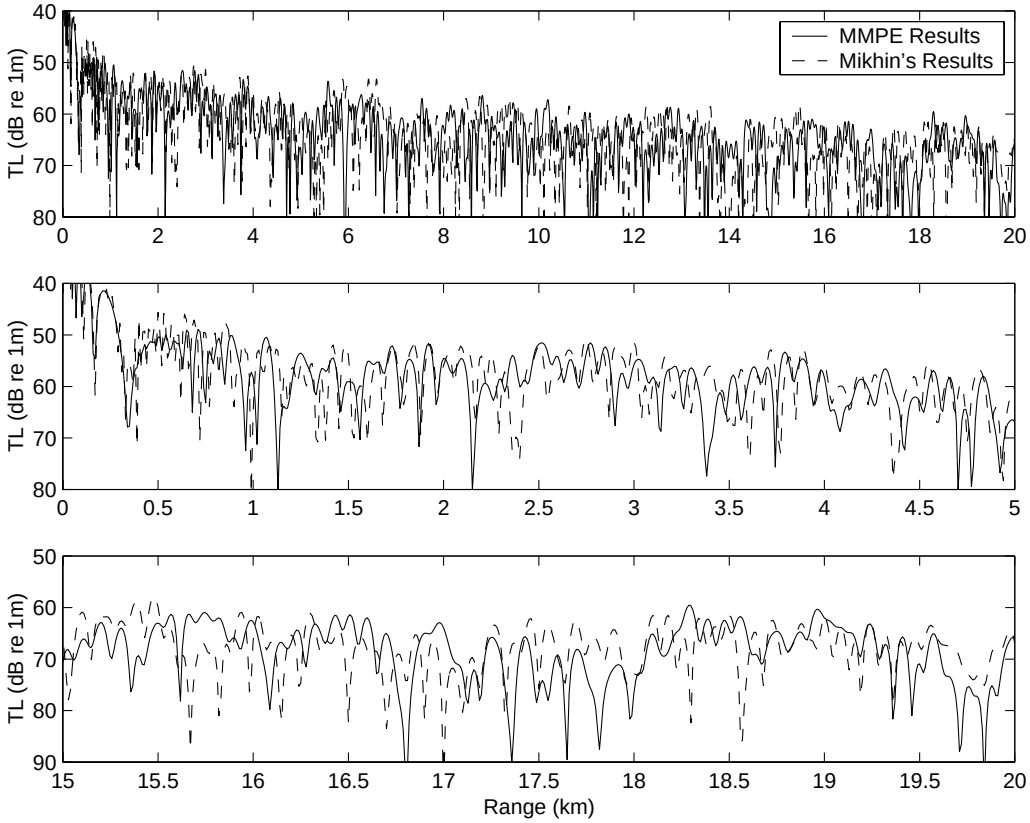

Figure 21: Comparison of optimal MMPE results with Mikhin's results for the IWc environment. The source corresponds to the 250 Hz CW source at 30 m depth.

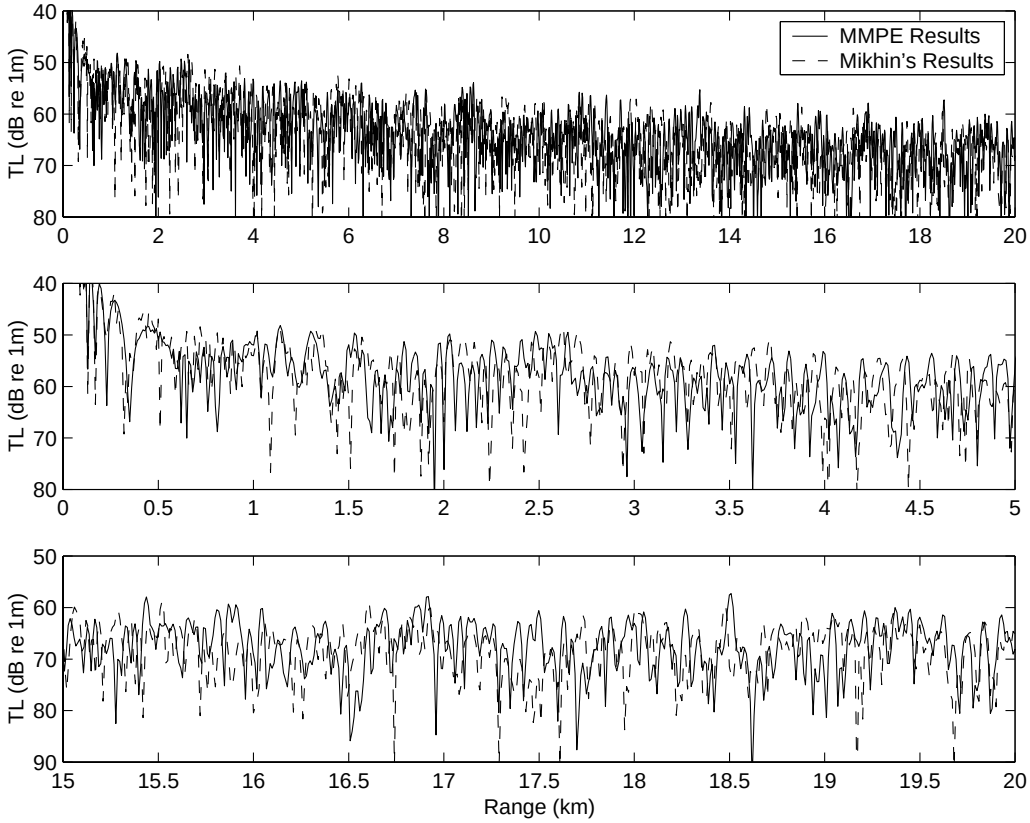

Figure 22: Comparison of optimal MMPE results with Mikhin's results for the IWc environment. The source corresponds to the 500 Hz CW source at 30 m depth.

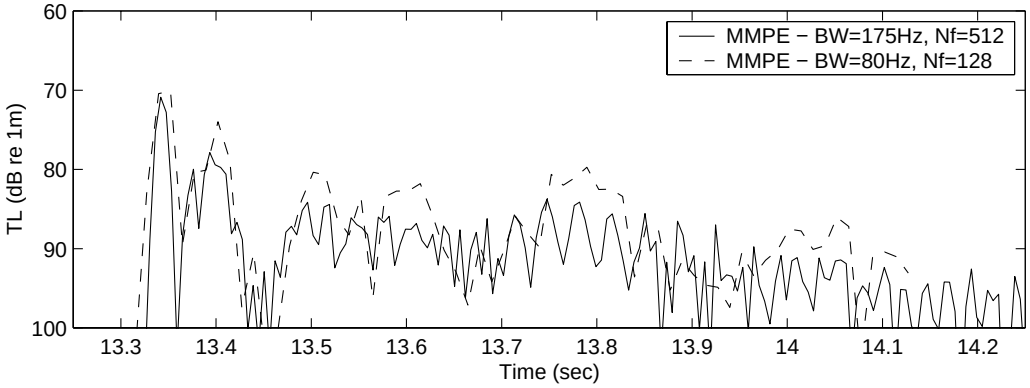

Figure 23: Comparison of MMPE results for different bandwidths of broadband pulse propagation in the FLATa environment. The source spectrum is modeled as a Hanning window with total width 175 Hz and 80 Hz, as indicated. The source depth is 30 m and the receiver is located 20 km away at depth 35 m.

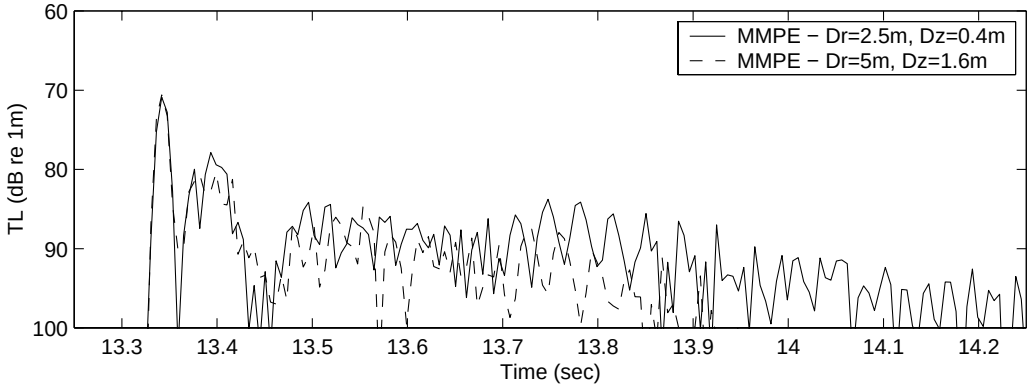

Figure 24: Comparison of the same broadband MMPE results for the FLATa case for different computational mesh sizes. Both source spectra are modeled as Hanning windows with total width 175 Hz.

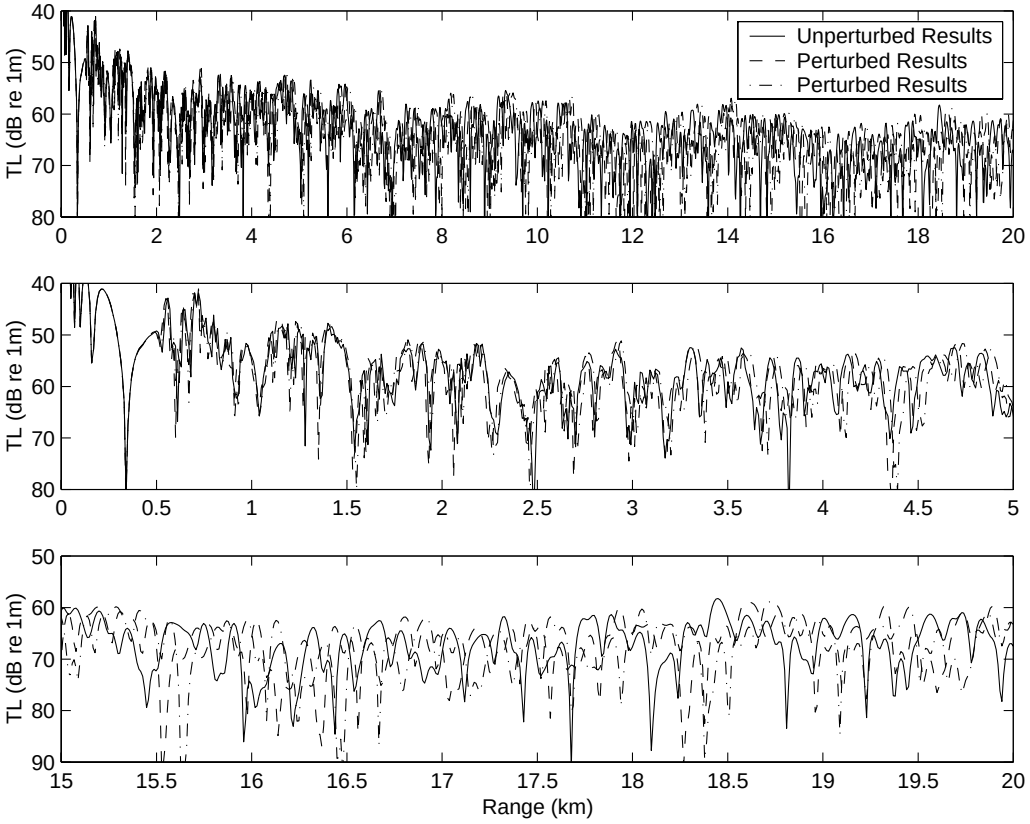

Figure 25: Comparison of MMPE results for the 250 Hz CW source in the FLATa environment. Two of the results were computed using perturbed environments to show variability caused by environmental uncertainty.